2020-10-01

The role of alongshore flows on inner surf and swash zone hydrodynamics on a dissipative beach

Puleo, JA

10.1016/j.csr.2020.104134
Continental Shelf Research
Elsevier BV

The Role of Alongshore Flows on Inner Surf and Swash Zone Hydrodynamics on a Dissipative Beach

Jack A. Puleo[1], Demetra Cristaudo[2], Alec Torres-Freyermuth[3], Gerd Masselink[4], Fengyan Shi[5]

[1]Professor and Associate Chair, Department of Civil and Environmental Engineering, University of Delaware, Newark, DE 19716, jpuleo@udel.edu, corresponding author

[2]PhD Candidate, Department of Civil and Environmental Engineering, University of Delaware, Newark, DE 19716, demetra@udel.edu

[3]Associate Professor, Laboratorio de Ingeniería y Procesos Costeros, Instituto de Ingeniería, Universidad Nacional Autónoma de México, Sisal, Yucatán, 97830, atorresf@iingen.unam.mx

[4]Professor, School of Biological and Marine Sciences, University of Plymouth, Drake Circus, Plymouth, Devon PL4 8AA, United Kingdom, gerd.masselink@plymouth.ac.uk

[5] Research Professor, Department of Civil and Environmental Engineering, University of Delaware, Newark, DE 19716, fyshi@udel.edu

Abstract

Cross-shore and alongshore velocities were measured over five high tide cycles in the swash and inner surf zones of a dissipative beach (significant wave height between 0.5 and 1.65 m; water levels between 0 and 0.87 m) using acoustic and electromagnetic current meters. Measurements are used to determine the importance of alongshore motions relative to cross-shore motions for bed shear stress; a parameter required for many sediment transport formulations. Velocities and water depths are infragravity dominated with running average (5 minutes) cross-shore and alongshore velocities being of similar magnitude near 0.25 m/s. Significant coherence squared between cross-shore velocity and water depth is found in an infragravity frequency range (0.0078 Hz to 0.024 Hz). A narrower infragravity frequency range (0.012 Hz to 0.022 Hz) of significant coherence squared is found between alongshore velocity and water depth. Near bed

velocity profiles at high spatial resolution indicate the mean profile of cross-shore or alongshore velocity for different relative cross-shore positions are nearly depth uniform, suggesting, on average, a well-mixed water column. Time-averaged onshore-directed depth-averaged velocities are nearly constant as a function of mean water depth, whereas time-averaged offshore-directed depth-averaged velocity magnitudes decrease with an increase in mean depth. In contrast, mean alongshore depth-averaged velocity magnitudes increase with depth regardless of the corresponding cross-shore motion and were always southerly-directed. These variations result from changes in breaking wave forcing location (i.e. relative cross-shore position). Near instantaneous velocity profile data are used to estimate friction coefficients and the bed shear stress through the Law of the Wall assumption. Mean friction coefficients for alongshore flows are similar to those obtained for cross-shore flows and values of ~ 0.02 are appropriate for all phases of flow. Alongshore bed shear stresses are the dominant bed shear stress component for over 27% of the samples implying an enhancement of total bed shear stress through incorporation of alongshore motions. Neglecting these alongshore processes (even if alongshore uniform) in cross-shore sediment transport models will lead to errors in predicted sediment transport rates.

Highlights

1) Cross-shore and alongshore flows in the swash/inner surf zones were analyzed
2) Alongshore flows need to be included in bed shear stress estimates
3) Friction coefficients for alongshore and cross-shore flows are similar
4) Despite flow complexity a friction factor of 0.02 can be used for bed shear stress

Keywords

Swash zone, Shear stress, velocity, foreshore, friction coefficients, logarithmic law

1.Introduction

Waves approaching the coast eventually break and transfer momentum into the water column. The organized wave motion is transformed into cross-shore and alongshore flows, low frequency motions, and turbulent bores inside the breaking region. Bores then propagate towards shore and may reform multiple times depending on the dissipative nature of the beach. The inner surf (loosely defined as continually submerged and depths less than ~ 1 m) and swash zones exist closer to the shoreline with the swash zone identified by intermittent submergence and flows over the foreshore (Butt and Russell, 2000; Masselink and Puleo, 2006). A distinction between dissipative and reflective beaches is commonly made comparing the steepness of the incident waves with the steepness of the beach profile. Dissipative beaches are characterized by a mild slope and a wider surf zone. Infragravity waves (low frequency motion) usually dominate the swash in such environments (Guza and Thornton, 1982; Holman, 1981; Hughes et al., 2014; Raubenheimer et al., 1995).

Substantial progress in the past decades has been achieved regarding knowledge of swash zone processes (Chardon-Maldonado et al., 2016). The 2nd International Workshop on Swash Zone Processes (Puleo and Torres-Freyermuth, 2016) highlighted the research advances and the shortcomings in swash zone processes research requiring more attention. One of the hydrodynamic topics identified was further investigation of the alongshore component of flow velocities. Variabilities in the alongshore flows may play a role in longer term beach evolution

74 dominated by mean wave conditions, particularly relevant in sea-breeze dominated conditions
75 (Masselink and Pattiaratchi, 1998; Torres-Freyermuth et al., 2017).

76 Bed shear stress mobilizes sediment and is included in sediment transport formulations. Bed
77 shear stress is estimated in field efforts from velocity measurements. Most prior studies have
78 focused solely on the cross-shore bed shear stress component arising from cross-shore velocity
79 (Butt et al., 2005; Masselink and Russell, 2006; Puleo et al., 2012; Raubenheimer, 2002). In
80 contrast, the alongshore component of flow velocity and associated bed shear stress is often
81 neglected. Yet, large alongshore flows in the swash zone have been reported (Austin et al., 2011;
82 Holland et al., 2001; Wang et al., 2002). For instance, maximum cross-shore and alongshore
83 flows during studies on sandy and gravel beaches were of the same magnitude, with alongshore
84 flows being more unidirectional rather than having a defined flow reversal as for cross-shore
85 flows. These large alongshore flows generate additional shear stress that could enhance cross-
86 shore sediment transport (Austin et al., 2011).

87

88 Advances in the modelling of swash zone processes has also been achieved (e.g. Briganti et al.,
89 2016) since early pioneering work (Hibberd and Peregrine, 1979; Ho and Meyer, 1962; Shen and
90 Meyer, 1963). Wave runup (Raubenheimer and Guza, 1996; Roelvink et al., 2018), cross-shore
91 velocities (O'Donoghue et al., 2010), boundary layer evolution (Pintado-Patino et al., 2015),
92 turbulence (Kim et al., 2017), and sediment transport (Incelli et al., 2016) have been investigated
93 with phase-resolving models. However, less effort (Chen and Briganti, 2006) has been devoted
94 to modeling swash zone alongshore flows. Moreover, Boussinesq and non-linear shallow water
95 equation models rely on friction coefficients, that may vary for cross-shore and alongshore

96 motion, to estimate bed shear stresses. Hence, further understanding of near bed processes during
97 alongshore flows is important for incorporation into predictive models.

98

99 The few aforementioned studies indicated the potential importance of alongshore flows on inner
100 surf and swash zone processes including bed shear stresses and sediment transport. However,
101 additional observations are needed to gain a better understanding of those processes. A field
102 experiment was conducted on a dissipative beach where detailed measurements of cross-shore
103 and alongshore flows were obtained in the inner surf and swash zones. The aim of this paper is to
104 quantify the relative magnitude of alongshore velocity, cross-shore and alongshore friction
105 coefficients, and the enhancement of total bed shear stress through incorporation of alongshore
106 motions with implications for altering cross-shore sediment transport.

107

108 2. Field Study

109 2.1 Experiment Site

110 A Beach Sediment Transport (BeST) study was conducted on Perran Beach in Perranporth,
111 Cornwall, United Kingdom (Figure 1). The study has been described in several other papers
112 (Inch et al., 2015; Puleo et al., 2014a), retaining the nomenclature and with brief details provided
113 here. The foreshore slope at Perran Beach is roughly 1:45 near mean high water and is composed
114 of sand with a median grain diameter, D_{50}, of 0.33 mm. Mean tidal range is over 5 m. The 3.5 km
115 long beach is bounded by headlands (Ligger and Droskyn Points) and trends roughly
116 North/South. Inner surf and swash motions are forced by North Atlantic swell and locally
117 generated seas. Offshore conditions were obtained from a Datawell buoy

(www.channelcoast.org; (50° 21' 11.34''N, 5° 10' 30.11''W) in approximately 10 m water depth at low tide.

The field experiment was conducted from October 09 to 15 in 2011, comprising 10 high tide cycles (Figure 2). Only Tides 4, 5, 7, 9, and 10 (see Puleo et al., 2014a) are retained in this study as the bed level was identifiable for the majority of these tide cycles (see Section 3.1). The high tide level, referenced to Ordnance Datum Newlyn (ODN), was between 2.98 m and 3.15 m (Figure 2A). The significant wave height, H_s, decreased from 1.65 m for Tide 4 to 0.75 m by Tide 10 (Figure 2B). The spectral peak wave period, T_p, ranged between 9.4 s and 15.2 s for the five tides retained (Figure 2C). Offshore wave angle was approximately shore normal with small variability (Figure 2D; relative to dashed line). Iribarren numbers (Iribarren and Nogales, 1949; $\xi = tan\beta / \sqrt{\left({H_0}/{L_0}\right)}$; where $tan\beta$ is the beach slope, and H_0 and L_0 are the offshore wave height and wave length (H_s and corresponding wave length used here); range from 0.2 to 0.4. Other surf similarity ($\epsilon = \frac{\pi}{\xi^2}$; Battjes, 1975) values roughly estimating breaking wave height by offshore wave height range from 19.6 to 78.5 and indicate dissipative conditions with dissipativeness increasing with increasing ϵ (Wright et al., 1982).

2.2 Field Sensor Deployment

A frame (45 m long) was constructed near the high tide line using scaffolding pipes pounded into the sand (Figure 3A). Sensors consisted of two Valeport Electromagnetic Current Meters (EM; only the lower EM used in this paper), a Nortek Profiling Velocimeter (PV), and a Druck PTX1830 pressure transducer (PT) for measuring water depth (Figure 3B). The EM measures cross-shore (u) and alongshore velocity (v) at a single elevation above the bed. The PV measures a vertical profile of u, v and the vertical velocity, w, at 0.001 m bin spacing over a range of 0.03

140 m. The velocity sensors were attached to a cross member located at x = -68.4 m in a local
141 coordinate system (Figure 4A), with the cross-shore coordinate (x) increasing onshore and
142 longshore coordinate (y) increasing to the north. The EM pair and PV were separated by 0.8 m in
143 the alongshore direction. The PT was buried below the EM pair and sampled at 4 Hz. The lower
144 EM was positioned at 0.03 m above the bed prior to each tidal inundation and set to sample at 4
145 Hz. The PV was positioned at 0.06 m above the bed prior to each tidal inundation and set to
146 sample at 100 Hz. The profiling range of the PV begins 0.04 m from the central transducer
147 meaning that the lower 0.01 m of the profiling range extends initially across the sediment
148 interface. The bottom-track mode of the PV was used during the study (at 2 Hz) to assist in bed
149 identification based on amplitudes of acoustic returns.

150 Sensors were cabled to recording computers contained in a field hut on the landward portion of
151 the beach. Computers were time synchronized using a GPS clock to update each computer clock
152 every second. Sensors were not triggered simultaneously. Data were subsequently interpolated to
153 the PV time.

154

155 ## 3. Data Collection and Analysis

156 ### 3.1 Surveying and Morphology

157 Beach profiles were collected adjacent to the scaffold frame and down the scaffold frame
158 centerline pre- and post-tide using an electronic total station (Figure 4A). Sensor position was
159 also surveyed providing an indication of the pre- and post-tide sensor elevation relative to the
160 bed. Beach elevations changed maximally 0.12 m over the study duration with largest changes
161 occurring well landward of the sensor location. Elevation changes pre- and post-tide (Figure 4B)

were maximally 0.03 m near the sensors (marked by the square symbol in Figure 4A). Larger intra-tide elevation changes were documented previously (Puleo et al., 2014b) and are shown in Section 4.1. Surficial sediment samples were collected for a portion of the beach profile and showed a progressive fining in grain size (D_{50} = 0.35 to 0.25 mm) in the landward direction (Figure 4C).

3.2 Quality Control

Knowledge of bed elevation is critical for identifying time-dependent sensor elevations and data to be used in later analyses. It is incorrect to assume the bed elevation changes linearly through the tide as related to pre- and post-survey measurements (Puleo et al., 2014b). Here, PV amplitude return data from the bottom track feature were used to identify the time-dependent bed elevation. The bed elevation is associated with high amplitude returns in the amplitude profile. The bed location is identified as the highest vertical location in the amplitude profile where a local maximum exceeds – 4 dB (Puleo et al., 2014b). No bed elevation was recorded when these two conditions were not met; most notably when the PV was landward of the active swash zone or the water level was below the sensor elevation. Gaps in the bed elevation time series were filled by linear interpolation. The average gap length was 19 s with a maximum gap length of 365 s. Bed elevations obtained using the PV compared favorably in a previous study to alternate methods using a conductivity concentration profiler and standard surveying techniques (Puleo et al., 2014b).

PT (0.01 – 0.04 m) elevation time series were estimated (assuming alongshore uniformity) using the PV-determined bed elevations interpolated to PT time and the initial distance between the PT

184 and local bed level. PT data were then corrected for atmospheric pressure and converted to water
185 depth, *h*, using a calibration curve determined in a laboratory calibration facility and subtracting
186 the PT elevation time series to obtain the actual water level above the bed. EM and PV sensor
187 elevations were adjusted similarly after interpolating *h* to their respective times. EM and PV
188 sensors use calibrations obtained from the manufacturer. The water depth was then used as a first
189 quality control measure where velocity data were removed when the water depth was less than
190 0.01 m above the sensor elevation. EM and PV data required additional quality control due to
191 potential emergence, submergence, and aeration that are known to induce noise (see review by
192 Chardon-Maldonado et al., 2016). EM data were removed from the record if the magnitude of
193 the velocity difference between adjacent records exceeded 0.5 m/s. PV data were removed from
194 the record when the beam correlation was less than 60% and/or the beam amplitudes were less
195 than -30 dB for at least two of the four beams (see also Puleo et al., 2012). The same velocity
196 difference criterion for the EM was also applied to PV data. Additionally, any velocity segments
197 that occurred for less than five samples were removed from the record. The last step involved
198 removing PV data located below the bed, where the bed elevation was described previously.

199 Other work using a small subset of these data identified individual swash events and performed
200 ensemble-averaging (Inch et al., 2015; Puleo et al., 2014b). Swash events on dissipative beaches
201 may be more difficult to define due to a dominance of low-frequency motions. The location of
202 the sensors also implies that data are sometimes located in the swash zone or the inner surf zone.
203 Thus, data in this paper were not divided for ensemble averaging nor generally demarcated as
204 being contained in the swash or inner surf zone. Instead data will be presented in relation to local
205 or mean water depth providing some indication of the relative cross-shore position of the
206 measurement (Austin et al., 2011; Masselink et al., 2005; Miles et al., 2006).

207

208 3.3 Bed Shear Stress Estimation

209 The bed shear stress, τ, is the main parameter used in energetics-based sediment transport
210 formulations (e.g. Bagnold, 1966; Bailard, 1981; Meyer-Peter and Muller, 1948) and swash zone
211 numerical models (Briganti et al., 2016). However, τ is difficult to quantify even for immobile
212 beds. Some approaches in mobile bed scenarios include the quadratic drag law (Barnes et al.,
213 2009; Masselink et al., 2009; Puleo et al., 2000), the von Karman-Prandtl relationship or Law of
214 the Wall (Austin et al., 2011; Cox et al., 2000; Inch et al., 2015; Miles et al., 2006; Puleo et al.,
215 2012), shear plates (Barnes et al., 2009; Jiang and Baldock 2015), hot film anemometers (Conley
216 and Griffin, 2004; Gust, 1988) or more recently the use of ferrofluids (Musumeci et al., 2018).
217 None are ideal and thus more simplified methods are often chosen, even though the assumptions
218 for using a particular approach may be violated.

219 Bed shear stress is obtained through the fundamental definition of the friction velocity as

220 $$\tau_x = \rho u_* |u_*|, \quad (1)$$

221 where subscript x denotes cross-shore, ρ is the fluid density, u_* is the friction velocity and | |
222 indicate magnitude to preserve direction of the bed shear stress. The friction velocity is obtained
223 through the Law of the Wall (von Karman, 1931), with drawbacks addressed in Section 5. The
224 Law of the Wall indicates a mean velocity profile of a fully developed, turbulent flow over a
225 fixed impermeable bed as

226 $$u(z) = \frac{u_*}{\kappa} ln\left(\frac{z}{z_0}\right), \quad (2)$$

where $u(z)$ is the cross-shore velocity profile, κ (= 0.4) is the von Karman's constant, z is the elevation above the instantaneous bed, and z_0 is the roughness height. Inner surf and swash zone flows occur over a mobile permeable bed in conditions of accelerating flow and/or flow where the turbulence is not fully developed. Yet, equation (2) has been used successfully in many past studies under similar conditions (e.g. Jensen et al. 1989; Austin et al. 2011; Kikkert et al. 2012; Puleo et al. 2012; Inch et al. 2015; O'Donoghue et al. 2016).

Bed shear stress time series should also contain an alongshore component even if the interest of a particular study is cross-shore only. The reason is that the total bed shear stress provides the mobilization force per area (at least in a bed load sense) for grains that can then be transported with a cross-shore component. Thus, the vector resultant bed shear stress magnitude becomes

$$\tau = \sqrt{\tau_x^2 + \tau_y^2}, \tag{3}$$

where τ_y is the alongshore component of bed shear stress arising from (1) and (2) using v_* and $v(z)$ respectively.

The quadratic drag law for cross-shore and alongshore flows, when velocity profile data are not obtained, is employed as

$$\tau_{DL,x} = \frac{1}{2}\rho c_{f,x} u_{DL}|u_{DL}|, \quad \tau_{DL,y} = \frac{1}{2}\rho c_{f,y} v_{DL}|v_{DL}|, \tag{4}$$

where the subscript DL implies drag law, $c_{f,x}$ and $c_{f,y}$ are empirical friction coefficients, and u_{DL} and v_{DL} are the cross-shore and alongshore velocity used in (4). Values for $c_{f,x}$ in the inner surf and swash zones of sandy coasts are typically in the range of 0.005 to 0.04 (e.g. Puleo and Holland 2001; Conley and Griffin 2004; Raubenheimer et al. 2004; Austin et al. 2011). Few studies have investigated $c_{f,y}$ (Austin et al., 2011), but found values similar to $c_{f,x}$. The value u_{DL}

248 (or v_{DL}) should be taken at the top of the boundary layer. In practice, u_{DL} is often taken from
249 wherever a current meter happens to be located independent of the varying elevation with respect
250 to the bed or boundary layer height due to both inability to adjust the sensor during a recording
251 interval and natural changes in the boundary layer structure during the swash or inner surf zone
252 event.

253 The friction coefficient can be determined when velocity profile data exist using equation (2) and
254 equation (4) as

255 $$c_{f,x} = \frac{2u_*|u_*|}{u_{DL}\,|u_{DL}|} \quad or \quad c_{f,y} = \frac{2v_*|v_*|}{v_{DL}\,|v_{DL}|}. \tag{5}$$

256

257 4. Results

258 4.1 Cross-shore and Alongshore Flows

259 Example swash zone and inner surf zone data from Tide 5 indicate similarities in depth (Figure
260 5A,B) and velocity magnitudes (Figure 5C-F). The temporal evolution of velocity components is
261 similar for both PV and EM. However, the PVs consistently predict a larger velocity magnitude
262 and display high-frequency fluctuations as compared to the EMs. Maximum onshore-directed
263 measured velocities for this example exceed 1 m/s whereas offshore-directed velocity
264 magnitudes approach 2 m/s for swash zone flows (Figure 5C). Maximum offshore-directed
265 velocities are less when the sensors are located in what would be defined as inner surf zone
266 (Figure 5D). Alongshore flows for this example are less than 0.5 m/s before increasing to nearly
267 1 m/s (Figure 5E) when the cross-shore flow is onshore-directed (Figure 5C between 2920 and
268 2930 s). Alongshore flow changes direction in the inner surf zone example where the flow depth

does not go to zero (Figure 5F). Here, the flow is northerly directed during offshore-directed cross-shore flow and then mostly southerly directed during onshore-directed cross-shore flow. The change in alongshore flow direction (and difference relative to Figure 5E) highlights the importance of local processes driving alongshore inner surf and swash motions; even if the offshore incident angle is fairly constant. Gaps in the time series occur when the water depth is below the sensor elevation and/or the other quality control criteria are not met (e.g. Figure 5D). Data removal is most obvious near time 2910 – 2920 s in Figure (5C,E), when the beach falls dry between swash events and near 7375 s in Figure (5D,F) when a turbulent bore passes the sensors.

A summary plot of the five retained tides is given in Figure 6. Five-minute block-averaged cross-shore velocities are generally offshore-directed (roughly -0.2 m/s) except during the beginning and ending of the tide (Figure 6B). Averaging only includes times when data exist, such that data gaps or times of no water depth do not skew the calculation. Offshore dominance is partially attributed to the sensor difficulty upon immersion and/or aerated flow during onshore-directed motion; a common problem in swash zone studies (Chardon-Maldonado et al., 2016). Velocities from the PV (blue; from the highest submerged bin) and EM (black) are similar except the EM is able to capture more of the offshore-directed flow as the tide level drops whereas the PV is skewed towards onshore flows as the tide level drops. Five-minute block-averaged alongshore flows are nearly always southerly-directed (Figure 6C), even though the offshore wave direction is often from south of shore normal possibly associated with surf zone morphology affecting wave refraction and spatial radiation stress gradients. Block-averaged alongshore flows are of the same magnitude of average cross-shore flows. Five-minute block-averaged bed elevations (Figure 6D) indicate change is less than 0.05 m over a tidal cycle.

292 Velocity spectra ($S_{u,PV}$, $S_{v,PV}$, $S_{u,EM}$, $S_{v,EM}$; for cross-shore and alongshore velocities measured by
293 the PV and EM, respectively) and depth spectra (S_h) were calculated to identify where the peak
294 energy resides and the level of infragravity energy contained in the signal (denoted, for example,
295 as $\%IG_{u,PV}$ to represent the cross-shore velocity from the PV). Discontinuous data were largely
296 avoided in the calculation by removing the first and last 15 minutes of each record. Spectra were
297 then calculated on time series interpolated to the PT time and over 2048 s de-trended, Hamming-
298 tapered segments with 50% overlap, band-averaged over five frequency bins (75 degrees of
299 freedom). Example spectra from Tide 10 indicate a broad spectral peak between roughly 0.007
300 Hz and 0.026 Hz (142.9 s and 38.5 s respectively; Figure 7; black squares) for all parameters
301 with a 95% confidence interval shown. Spectra for other tides are similar (not shown) as are the
302 spectral peaks (Table 1). Infragravity energy may be considered to occur at frequencies below
303 0.05 Hz (20 s). At least 71% and 72% of the cross-shore and alongshore spectral energy density,
304 respectively, are contained in the infragravity band (Table 2). A minimum of 62% of the depth
305 spectral energy density is considered to be in the infragravity band; all as expected for a
306 dissipative beach. Spectral rolloff for cross-shore velocities follows the f^{-2} slope over several
307 decades of frequency (Figure 7). The slope is flatter near the incident peak than might be
308 expected for flows in the surf zone (Foster et al., 2000; Smyth and Hay, 2003) and for runup on
309 dissipative beaches (Hughes et al., 2014).

310 Two-dimensional histograms were constructed for the near-bed velocities and corresponding
311 water depth for the five retained tides (Figure 8). Distributions for cross-shore velocity (Figure
312 8A,C) have a similar shape and are skewed offshore near the bed and onshore away from the
313 bed. Cross-shore velocity magnitudes are maximal with the greatest percent occurrence at depths
314 of 0.1 m. There is a secondary peak of percent occurrence near a depth of 0.2 m where the cross-

315 shore velocity is near zero (more obvious in Figure 8C). This peak in occurrence is likely
316 attributed to the most common depth for swash flow reversal. Large, onshore-directed cross-
317 shore velocities (e.g. $u > 0.5$ m/s) when viewed in this fashion are not common, but are nearly
318 uniform in occurrence with respect to depth identified by the vertical contour shading. Large,
319 offshore-directed cross-shore velocity magnitudes exhibit similar contour shading for the PV
320 measurements (Figure 8A), but not the EM measurements (Figure 8C). Instead, there is a
321 tendency for offshore-directed velocities to increase with decreasing water depth likely attributed
322 to backwash flows. Alongshore velocity histograms (Figure 8B,D) are skewed slightly negative
323 (southerly flow) with both measurement types having a peak occurrence (2% to 3%) near zero
324 velocity. Maximum alongshore velocity magnitudes exceed 0.5 m/s, but with frequency of
325 occurrence < 0.1%. Contour shading for northerly and southerly directed flow is nearly vertical
326 indicating there is weak preferential direction or magnitude as a function of depth from a percent
327 occurrence viewpoint. Mean velocities as a function of depth are also identified by the gray
328 curves. Cross-shore mean velocities are onshore-directed for deeper water and offshore-directed
329 for shallower water (less than ~ 0.35 m). Mean alongshore velocities are southerly directed
330 regardless of depth.

331

332 Cross-spectral analysis was performed over 2048 s de-trended, Hamming-tapered segments with
333 50% overlap, band-averaged over five frequency bins to quantify squared coherence between the
334 different velocity measurements and local water depth (Figure 9). The squared coherence is
335 quantified using the coincident, quadrature the one-sided spectra for the quantities of interest (see
336 Emery and Thomson, 2001). Averaged data for the five tides are shown with shading indicating
337 minimum and maximum values. The squared coherence for depth to cross-shore velocity (PV or

EM) exceeds the 95% confidence level (dashed line) beginning at frequencies 0.0078 Hz (PV, Figure 9A; where the solid black curve crosses the horizontal dotted line) and 0.0063 Hz (EM, Figure 9B). The largest squared coherence for depth to cross-shore velocity occurs for frequencies 0.0189 Hz (PV) and 0.0161 Hz (EM) well below the incident wave frequency of roughly 0.1 Hz. Coherence squared between cross-shore to alongshore velocity or depth to alongshore velocity is weak with few instances of coherence squared exceeding the 95% confidence level (between frequencies of 0.0115 Hz to 0.0215 Hz; again well below the incident wave frequency). Not surprisingly, the squared coherence peaks occur at or near the peaks in spectral energy for the corresponding parameters (Figure 7 and Table 1). Phase estimates when coherence squared exceeds the 95% confidence level corresponding to the cross spectra are shown in Figures (9C,D). There is no discernible pattern for the phases between cross-shore and alongshore velocity (or depth and alongshore velocity) except that they tend to be negative meaning *v* lags *u* in the infragravity band. The water depth is roughly 90 degrees out of phase with the cross-shore velocity (*u* lags *h*) for frequencies between roughly 0.009 Hz and 0.027 Hz indicative of standing or partially standing wave motions (Figure 9C,D). The lag rapidly approaches zero for high frequencies.

4.2 Velocity Profiles and Depth-Averaged Velocities

Velocity presented thus far was obtained from the EM or from the highest submerged bin of the PV. Velocity profiles provide an indication of boundary layer structure and enable estimation of the shear stress through equation (2). Figure 10 shows a time series excerpt of an infragravity event from Tide 07. The color variations correspond to the vertical lines in Figure (10B) for temporal sampling location. The water depth exceeds 0.5 m and begins and ends near zero depth

(swash zone). PV (blue; highest submerged bin) and EM (black) cross-shore velocities show the incident band oscillations in velocity occurring within the longer duration event. Onshore-directed velocities approach 1 m/s while maximum offshore-directed velocity magnitudes exceed 1.5 m/s. The corresponding alongshore flows (PV as cyan from highest submerged bin; EM as grey) also oscillate on incident band time scales, but are largely negative (southerly directed) for the duration of the infragravity motion. Maximum alongshore velocity magnitudes exceed 1 m/s. Cross-shore (Figure 10C) and alongshore (Figure 10D) velocity profiles decrease towards the bed indicative of the boundary layer. The decrease is subtle in some instances especially for alongshore flow. Alongshore velocities near cross-shore flow reversal may still have a non-negligible component (near time of 6180 s) or be large (near time of 6135 s).

Velocity records from the five retained tides were interrogated for different depth bins (Table 3) and plotted as a function of elevation separated by onshore- and offshore-directed cross-shore flow (Figure 11, 12). Relating velocities to mean depth is akin to comparing velocities based on relative cross-shore position due the fixed sensor position and migrating tide level (Masselink et al., 2009; Miles et al., 2006). Thus, bins *h1* (0 – 0.1 m] and *h2* (0.1 – 0.2 m] are inferred to be swash zone with the depth bins inner surf zone. The mean velocity, $\langle u \rangle$ or $\langle v \rangle$, at each elevation is shown as a filled circle with the diameter corresponding to the number of data points. Grey shading indicates the standard deviation of velocity at a particular elevation. Velocities are offset horizontally by 1 m/s for visual clarity. The majority of data for onshore-directed cross-shore velocity occur for depth bins h_2, h_3, and h_4. The number of data points for larger depths and towards the top of the profile decreases drastically such that the shape near the top of the profile is governed by less than 100 measurements. The characteristics for alongshore velocity profiles are similar except that the profiles appear to have more depth uniformity (Figure 12).

384

385 The degree of uniformity of the mean velocity profiles is calculated as (O'Donoghue et al., 2010)

386 $$B = \left[\frac{1}{d}\sum_0^d [< u > (z, h_i) - \overline{< u >}\,(h_i)]^2\,\Delta z\right]^{\frac{1}{2}}, \quad (6)$$

387 where as before $< >$ imply average over temporal samples, the overbar implies depth average, *d*
388 is depth over which the averaging occurs (here 0.02 m), Δz is the vertical bin spacing for velocity
389 measurements (here 0.001 m), and *i* identifies the different depth bins. Non-uniformity values
390 over the lower 0.02 m of the water column, are rarely larger than 0.1 m/s (Table 3) with the
391 exception of several of the profiles for the larger depth bins. The small *B* values indicate that the
392 mean profiles are indeed nearly depth uniform even though the instantaneous profiles show a
393 decrease in the velocity towards the bed indicative of boundary layer structure.

394 The mean of the depth-averaged velocities, $< \bar{u} >$ and $< \bar{v} >$ show some similarity and some
395 variability as a function of depth bin (Figure 13). Mean depth-averaged onshore-directed cross-
396 shore velocity is nearly constant for all depth bins with a similar variability (one standard
397 deviation shown either side of symbol). The offshore-directed cross-shore velocity decreases in
398 magnitude as the depth increases likely as the flow regime goes from swash processes to inner
399 surf zone processes. The standard deviation also decreases with an increase in depth bin. Mean
400 depth-averaged alongshore velocities corresponding to onshore-directed (black) and offshore-
401 directed (gray) cross-shore velocities show similar trends relative to each other. Alongshore
402 velocities are smallest at the smaller depth bins (mean of near zero) and increase almost linearly
403 with increasing depth reflecting the transition from swash zone to inner surf zone flows.
404 Alongshore velocities are found to have larger magnitude during the cross-shore velocities that
405 are off-shore directed.

406

407 4.3 Bed Shear Stress and Friction

408 The same time series excerpt is used as an example for the quantification of bed shear stress
409 from PV data (Figure 14). Bed shear stresses are quantified through equation (1 and 2). Velocity
410 profiles are block-averaged over 0.05 s to smooth over some of the turbulent fluctuations. The
411 friction velocity is estimated through a least squares regression procedure between the velocity
412 profile data and the *ln*(z), where *ln* is the natural logarithm. The square of the correlation
413 coefficient is used to determine model fit. Fits with squared correlation coefficient less than 0.7
414 are rejected, meaning the profile does not follow well the expected shape. Other cutoff values
415 ranging from 0.7 to 0.9 have been used in laboratory an field studies (Inch et al., 2015;
416 O'Donoghue et al., 2010; Puleo et al., 2014a, 2012) with a smaller value, as chosen here, being
417 more conservative. The slope of the regression for the accepted fits is multiplied by the von
418 Karman's constant (= 0.4) to yield the friction velocity and hence bed shear stress. The cross-
419 shore bed shear stress tends to dominate the alongshore bed shear stress, but there are many
420 instances where the two values are of similar magnitude (Figure 14B). The potential dominance
421 of τ_y can be highlighted by the ratio τ_y/τ (Figure 14B; grey curve). Ratio magnitudes greater
422 than $1/\sqrt{2}$ (= 0.707) indicate the bed shear stress is dominated by the alongshore component.
423 There are instances in the example excerpt where the alongshore component of bed shear stress
424 is of equal importance (e.g. between time of 6145 s to 6157 s) or larger than the cross-shore
425 component, τ_x.

426 A two-dimensional histogram is created to determine the ratio of the alongshore bed shear stress
427 to total bed shear stress as related to water depth for data from all five tides (Figure 14C). The

alongshore bed shear stress is the dominant component for 27.3% of the samples relative to the total bed shear stress. The percent occurrence of alongshore dominance skews towards southerly-directed flows. The largest percent occurrence is located at a depth of 0.13 m and calculated bed shear stress ratio of -0.18 suggesting that the most common scenario for the conditions during the study were for the cross-shore component of bed shear stress to represent just over 80% of the total bed shear stress magnitude. The alongshore component of bed shear stress independent of water depth is dominant 24% of the time for northerly-directed flow and 26% of the time for southerly-directed flow (not shown). The 50th percentile, independent of water depth, occurs for ${\tau_{y,north}}/{\tau} = 0.38$ and ${|\tau_{y,south}|}/{\tau} = 0.40$ (not shown).

Friction coefficients were calculated using equation (5). Values were retained only when the velocity magnitude in the denominator exceeded 0.1 m/s to negate dividing by a small number and causing $c_{f,x}$ or $c_{f,y}$ to trend towards infinity. Friction coefficients determined using cross-shore velocities had a larger percent occurrence for $c_{f,x} < 0.01$ and a smaller percent occurrence for larger $c_{f,x}$ regardless of flow direction. Friction coefficient statistics are 0.024 ± 0.035 (mean ± standard deviation) and 0.029 ± 0.036 for onshore flows and alongshore flows, respectively, when cross-shore flows are onshore-directed. Friction coefficients are similar for corresponding motion when flows are offshore-directed as 0.027 ± 0.033 and 0.035 ± 0.034, respectively. Mean friction coefficients are commensurate with those found in many other studies on sandy beaches (e.g. Puleo and Holland 2001; Raubenheimer et al. 2004).

450

451 5. Discussion

452 5.1 Cross-shore and Alongshore Velocities

453 The data collected on a dissipative beach during the BeST study indicate the importance of
454 alongshore flows in the inner surf and swash zones. Recorded alongshore flow magnitudes were
455 often of similar magnitude and showed variability during the tidal cycle. Mean alongshore and
456 cross-shore velocity profiles were nearly depth uniform over the lower 0.02 m of the water
457 column with standard deviations on the order of 0.5 m/s. Near uniformity of the temporal mean
458 profile enabled analysis of the depth-averaged mean velocity as a function of mean water depth.
459 Mean depth-averaged, cross-shore velocity magnitudes were greatest for offshore-directed flow
460 as the depth became shallower (Figure 13A). These flows are indicative of swash processes
461 where the thinning backwash flows generally increase in magnitude with flow duration under the
462 influence of gravity. The same velocity parameter for onshore-directed flow showed less
463 relationship with depth, but with a small increase (< 15%) as depths increased. There are two
464 likely reasons: 1) Onshore flows in the inner surf zone under bores can be large and the
465 submerged current meter is able to capture these flows with less difficulty being away from the
466 aerated portion; 2) Shallow flows depths for onshore-directed motion are linked with weak
467 swash motion, an aerated flow and/or a current meter that is instantaneously submerged, all
468 processes leading to less retained velocities and perhaps a smaller mean depth-averaged flow.

469 Mean alongshore depth-averaged flow velocities (Figure 13B) show similar trends regardless of
470 cross-shore flow motion. Alongshore flows are weakest and trend to zero as the depth shallows;
471 towards the shoreline in the swash zone. Alongshore flows for greater water depths are more

likely related to radiation stress gradients associated with inhomogeneous surf zone morphology rather than strictly oblique swash motion. Mean depth-averaged alongshore flows approach -0.5 m/s when cross-shore motion is offshore-directed and -0.25 m/s when cross-shore motion is onshore-directed. Larger alongshore flows during off-shore directed motion indicate the flows that impinge the beach at an angle and return at a similar or larger angle when in the inner surf zone. Swash motions are normally thought to have a potential for an alongshore component during onshore-directed motion (e.g. Asano 1996), but the flow beginning from rest may have a smaller alongshore component when the cross-shore motion is offshore-directed.

5.2 Bed Shear Stress and Effect on Sediment Transport

The bed shear stress is the major mobilization term in most sediment transport models (Bagnold, 1966; Meyer-Peter and Muller, 1948), but no widely adopted bed shear stress sensor exists. Field based hot film approaches (Conley and Griffin 2004) require an impermeable, fixed deployment device that may alter the flow field and laboratory-based shear sensors, even for mobile beds (Jiang and Baldock, 2015), have yet to be deployed in the field. Thus, calculations based on the local velocity field are often employed. The two most common approaches are the Law of the Wall relationship (Kikkert et al. 2012, 2013; Puleo et al. 2012, many others) and quadratic drag law (Puleo et al. 2000; Barnes et al. 2009; Masselink et al. 2009, many others). Both approaches have issues in the nearshore where underlying assumptions are violated (e.g. O'Donoghue et al. 2010). The Law of the Wall was derived for fully turbulent, steady flow over a roughened fixed bed. Inner surf and swash zone flows are unsteady and pass through flow reversal where the flow turbulence can vary considerable depending on flow type. The bed within the inner surf and swash zone is nearly always in motion often through sheet flow processes (Lanckriet et al., 2014; Puleo et al., 2015, 2014a). There is no guarantee the velocity profile will have a logarithmic

shape through all flow phases especially near flow reversal. Use of the Law of the Wall requires identifying the elevation over which to carry the analysis (here over up to 0.03 m consistent with some prior field studies; Austin et al. 2011; Puleo et al. 2012) and what level of fit between theory and measurement is deemed acceptable (here a squared correlation coefficient of 0.7, lower than for laboratory studies on impermeable slopes; O'Donoghue et al. 2010). Finally, the elevation from which velocity is extracted is critical to obtaining robust results (Puleo et al., 2014b) where elevations errors of only 0.001 m can lead to bed shear stress errors on the order of 100%. The quadratic drag law is more straightforward to implement. The velocity used in the formulation should come from the free stream, but the concept of a free stream velocity under a broken bore or for interacting swash and inner surf zone flows is problematic. Further, most velocity field measurements are obtained from a single current meter where the elevation above the bed (and with respect to the boundary layer height) varies on time scales much shorter than the wave period. Thus, the velocity is generally used from wherever if happens to be collected.

Bed shear stresses were estimated in this work using the Law of the Wall due to the availability of dense near-bed velocity profile data that are uncommon in most field studies. Application of the approach for both flow components showed that the alongshore component cannot be neglected and a full bed shear stress term must be quantified if sediment transport estimates are to be more robust. The alongshore component of bed shear stress was dominant for > 25% of the retained data and even when not dominant still represented a non-negligible portion of the total bed shear stress.

517 The majority of sediment transport models used in the inner surf and swash zone rely solely on
518 the cross-shore component of bed shear stress. But, using only the cross-shore bed shear stress to
519 estimate cross-shore sediment transport will underpredict the actual sediment transport
520 magnitude. As an example, τ (and hence cross-shore sediment transport) increases by 12% when
521 $\tau_y = 0.5\tau_x$ and by 123% when $\tau_y = 2\tau_x$; equivalent to $\frac{\tau_y}{\tau} = 0.57$ and $\frac{\tau_y}{\tau} = 0.89$ respectively.
522 The implications for disregarding alongshore bed shear stress on steeper beaches with a large
523 oblique offshore incidence angle may be more important due to a narrower surf zone.

524 The beach profile changed little during the experiment and was mostly alongshore uniform near
525 the sensor location (identified from additional cross-shore profiles; not shown) implying small
526 sediment transport gradients. Thus, the cumulative bed shear stress from which the transport
527 gradients may be estimated can provide additional indication on the importance of the
528 alongshore bed shear stress contribution. Bed shear stresses for the 5 tides were summed
529 cumulatively either incorporating (-5.06 x 10^4 N/m^2) or neglecting (-1.14 x10^5 N/m^2) the
530 alongshore component. The simple calculation would indicate a predicted net offshore transport
531 with the value incorporating both bed shear stress components being 36% smaller and more
532 commensurate with observed morphology.

533

534 5.3 Friction Coefficient

535 Comparisons between the Law of the Wall and the quadratic drag law were used to infer a
536 friction coefficient. Friction coefficient estimates in this study are similar to those estimated on
537 many other sandy beaches (e.g. Puleo and Holland 2001; Raubenheimer et al. 2004) with similar
538 grain sizes. The large standard deviation is indicative of the variability in estimating the friction

539 velocity (bed shear stress) from the Law of the Wall and the velocity profile and comparing it to
540 the bed shear stress obtained from velocity measured at a single elevation.

541

542 Austin et al. (2011) find a relationship between the friction coefficient and the Nikuradse
543 roughness length normalized by depth. Conley and Griffin (2004) find a weak relationship
544 between the friction coefficient and the inverse of the Reynolds number. Both findings suggest c_f
545 can be estimated from flow parameters and other descriptors, where c_f is a general variable
546 defining a friction coefficient. Several well-known formulations exist to estimate c_f based on
547 flow parameters. One incorporates the roughness and excursion amplitude (Swart, 1974) and the
548 other incorporates water depth and Reynolds number (Colebrook, 1939). The Swart approach is
549 less desirable because it requires identifying an excursion amplitude that changes with velocity
550 and inner surf zone wave period or swash duration. Quantifying the roughness is less
551 problematic, if the bed is nearly immobile, and is usually defined as some constant times the
552 median grain diameter. Bed roughness (and indeed friction) is more complicated under sheet
553 flow conditions (Wilson, 1989a, 1989b). The Colebrook equation is

554 $$\frac{1}{\sqrt{c_f}} = -K_1 log\left(\frac{k_s}{K_2 R_h} + \frac{K_3}{4Re\sqrt{c_f}}\right), \quad (7)$$

555 where k_s is the bed surface roughness, R_h is the hydraulic radius, Re is the Reynolds number and
556 K_1, K_2, and K_3 are coefficients depending on flow conditions (Chen, 2002). Coefficient values for
557 a full circular pipe are often adopted. Here, values of $K_1 = 2.03$, $K_2 = 11.09$, and $K_3 = 3.41$
558 (Keulegan, 1938) for a wide channel are used. Friction coefficient values change little varying
559 the K coefficients (Chen, 2002) obtained from different studies.

560 Equation (7) requires iteration to identify the friction coefficient, a fully turbulent flow, and a
561 fully developed boundary layer (see O'Donoghue et al. 2010), conditions that are often violated
562 in the inner surf and swash zones. Comparisons between $c_{f,x}$ and $c_{f,y}$ obtained from equation (5)
563 and those from equation (7) are shown in Figure (15). There is little variability in the friction
564 coefficient obtained from the Colebrook approach with values constrained largely (99% for
565 cross-shore and 92% of alongshore) between 0.008 and 0.03 and with a mean ± standard
566 deviation of 0.021 ± 0.003 and 0.022 ± 0.008 for cross-shore and alongshore flows respectively
567 (Figure 15). Friction coefficient values near 0.02 match well estimates used/found in previous
568 studies.

569 Bed shear stresses were re-calculated based on mean c_f from the Colebrook equation (= 0.021)
570 and the quadratic draw law (equation 5; velocity from the highest bin) to determine similarity
571 with bed shear stresses identified from the Law of the Wall (Figure 16). There is large scatter
572 between the bed shear stress estimates for both cross-shore and alongshore motions. The scatter
573 is commensurate with the scatter of c_f (Figure 15) with many points being located outside a
574 factor of 2 (Figure 16; dashed blue lines). O'Donoghue et al. (2016) also make this comparison
575 for laboratory data and find more data located within a factor of 2. However, comparisons were
576 for Law of the Wall bed shear stress from a fixed, coarse grained beach (mm and larger sized
577 particles) to drag law bed shear stress from the same hydrodynamic forcing but over mobile
578 beds. The results here and previous comparisons do not indicate readily which estimate is more
579 appropriate for quantifying bed shear stress in the inner surf and swash zones, especially
580 considering vertical mixing owing to wave breaking or turbulent bores is not explicitly
581 considered in either approach. However, the simplicity in using the quadratic drag law and lack

of need for a velocity profile may favor that approach for bed shear stress in most laboratory and field-based studies of inner surf and swash zone flows.

6. Conclusion

High resolution cross-shore and alongshore velocity profiles were collected in the swash and inner surf zones of a dissipative beach. Velocities were infragravity dominated with a wide frequency range of significant coherence squared between cross-shore velocity and water depth with roughly 90 degrees phase lag from 0.0078 Hz to roughly 0.024 Hz. The range of significant coherence squared between alongshore velocity and water depth was narrower (0.012 Hz to 0.022 Hz) with no discernible trend in phase lag. Cross-shore and alongshore bed shear stress were estimated by applying the Law of the Wall to the velocity profile data. Bed shear stress magnitudes were commensurate with past studies and exceeded 15 N/m^2. The alongshore bed shear stress relative to the total bed shear stress magnitude was dominant greater than 28% of the time. Friction coefficients obtained from the law of the Wall and the quadratic drag law were commensurate with many past studies on sandy beaches, but did not compare well to those estimated from the Colebrook equation. The weak comparison indicates the friction coefficient on during this study was not strongly related to water depth or Reynolds Number. The Law of the Wall, quadratic drag law and Colebrook equation have assumptions that are at times violated in the swash and inner surf zones requiring improved approaches for estimating friction and bed shear stress. The findings indicate the alongshore component of bed shear stress cannot be ignored even if the particular interest is for cross-shore processes only.

604 Acknowledgment

605 Funding for this work was provided by the National Science Foundation (Grant No. OCE-
606 1756714). Support for the field effort was provided by the Natural Environmental Research
607 Council (Grant NE/G007543/1), an Australian Research Council Discovery Project
608 (DP110101176), the US-UK Fulbright Commission, and the University of Delaware. The
609 authors acknowledge the field assistance of M. Austin, D. Buscombe, C. Blenkinsopp, D.
610 Conley, P. Ganderton, A. Jane, L. Joia, T. Lanckriet, R. McCall, A. McIver, L. Melo De
611 Almeida, T. Poate, B. Pronenca, C. Rosario, T. Scott, M. Sheridan, and I. Turner. Two reviewers
612 helped to improve the clarity of this manuscript.

613

614 References

615

616 Asano, T., 1996. Sediment transport in swash zone under obliquely incident waves, in: Edge,
617 B.L. (Ed.), Presented at the Proceedings of the 25th International Conference on Coastal
618 Engineering, ASCE, pp. 3770–3781.
619 Austin, M.J., Masselink, G., Russell, P., Turner, I., Blenkinsopp, C., 2011. Alongshore fluid
620 motions in the swash zone of a sandy and gravel beach. Coast. Eng. 58, 690–705.
621 Bagnold, R.A., 1966. An approach to the sediment transport problem from general physics
622 (Professional Paper No. 422– I). U.S. Geological Survey, Washington, DC.
623 Bailard, J.A., 1981. An energetics total load sediment transport model for a plane sloping beach.
624 J. Geophys. Res. 86, 938–954.
625 Barnes, M.P., O'Donoghue, T.O., Alsina, J.M., Baldock, T.E., 2009. Direct bed shear stress
626 measurements in bore-driven swash. Coast. Eng. 853–867.
627 Briganti, R., Torres-Freyermuth, A., Baldock, T.E., Brocchini, M., Dodd, N., Hsu, T.J., Jiang, Z.,
628 Kim, Y., Pintado-Patino, J.C., Postacchini, M., 2016. Advances in numerical modelling
629 of swash zone dynamics. Coast. Eng. 115, 26–41.
630 https://doi.org/10.1016/j.coastaleng.2016.05.001
631 Butt, T., Russell, P., 2000. Hydrodynamics and cross-shore sediment transport in the swash-
632 zone of natural beaches: A review. J. Coast. Res. 16, 255–268.
633 Butt, T., Russell, P., Puleo, J.A., Masselink, G., 2005. The application of Bagnold-type sediment
634 transport models in the swash zone. J. Coast. Res. 21, 887–895.
635 Chardon-Maldonado, P., Pintado-Patino, J.C., Puleo, J.A., 2016. Advances in swash-zone
636 research: Small-scale hydrodynamic and sediment transport processes. Coast. Eng. 115,
637 8–25.
638 Chen, B.C.Y., 2002. Open Channel Flow Resistance. J. Hydraul. Eng. 128, 20–39.
639 Chen, Q., Briganti, R., 2006. Numerical modeling of alongshore surf and swash zone currents,
640 in: Proceedings of the 30th International Conference on Coastal Engineering. World
641 Scientific, San Diego, CA, pp. 1040–1052.
642 Colebrook, C.F., 1939. Turbulent flow in pipes, with particular reference to the transition region
643 between the smooth and rough pipe laws. J. Inst. Civ. Eng. 11, 133–156.
644 Conley, D.C., Griffin, J.G., 2004. Direct measurements of bed stress under swash in the field. J.
645 Geophys. Res. 109, C03050, doi.10129/2003JC001899.
646 Cox, D.T., Hobensack, W.A., Sukumaran, A., 2000. Bottom stress in the inner surf and swash
647 zone, in: Edge, B. (Ed.), . Presented at the Proceedings of the 27th International
648 Conference on Coastal Engineering, ASCE, pp. 108–119.
649 Emery, W.J., Thomson, R.E., 2001. Data Analysis Methods in Physical Oceanography. Elsevier,
650 Amsterdam.
651 Foster, D.L., Beach, R.A., Holman, R.A., 2000. Field observations of the wave bottom boundary
652 layer. J. Geophys. Res. 105, 19631–19647.
653 Gust, G., 1988. Skin friction probes for field applications. J. Geophys. Res. 93, 14121–14132.
654 Guza, R.T., Thornton, E.B., 1982. Swash oscillations on a natural beach. J. Geophys. Res. 87,
655 483–491.
656 Hibberd, S., Peregrine, D.H., 1979. Surf and run-up on a beach: a uniform bore. J. Fluid Mech.
657 95, 323–345.

Ho, D.V., Meyer, R.E., 1962. Climb of a bore on a beach: Part 1, Uniform beach slope. J. Fluid Mech. 14, 305–318.
Holland, K.T., Puleo, J.A., Kooney, T., 2001. Quantification of swash flows using video-based particle image velocimetry. Coast. Eng. 44, 65–77.
Holman, R.A., 1981. Infragravity energy in the surf zone. J. Geophys. Res. 86, 6442–6450.
Hughes, M.G., Aagaard, T., Baldock, T.E., Power, H.E., 2014. Spectral signatures for swash on reflective, intermediate and dissipative beaches. Mar. Geol. 355, 88–97.
Incelli, G., Dodd, N., Blenkinsopp, C., Zhu, F., Briganti, R., 2016. Morphodynamical modeling of field-scale swash events. Coast. Eng. 115, 42–57.
Inch, K., Masselink, G., Puleo, J.A., Russell, P., Conley, D.C., 2015. Vertical structure of near-bed cross-shore flow velocities in the swash zone of a dissipative beach. Cont. Shelf Res. https://doi.org/dx.doi.org/10.1016/j.csr.2015.04.006
Iribarren, C.R., Nogales, C., 1949. Protection des ports. Presented at the XVIIth Int. Nav. Congress, pp. 31–80.
Jensen, B.L., Sumer, B.M., Fredsoe, J., 1989. Turbulent oscillatory boundary layers at high Reynolds numbers. J. Fluid Mech. 206, 265–297.
Jiang, Z., Baldock, T.E., 2015. Direct bed shear measurements under loose bed swash flows. Coast. Eng. 100, 67–76.
Keulegan, G.H., 1938. Laws of turbulent flow in open channels. J. Natl. Bur. Stand. 21, 707–741.
Kikkert, G.A., O'Donoghue, T.O., Pokrajac, D., Dodd, N., 2012. Experimental study of bore-driven swash hydrodynamics on impermeable rough slopes. Coast. Eng. 60, 149–166. https://doi.org/10.1016/j.coastaleng.2011.09.006
Kikkert, G.A., Pokrajac, D., O'Donoghue, T., Steenhauer, K., 2013. Experimental study of bore-driven swash hydrodynamics on permeable rough slopes. Coast. Eng. 79, 42–56.
Kim, Y., Zhou, Z., Hsu, T.-J., Puleo, J.A., 2017. Large eddy simulation of dam-break driven swash on a rough planar beach. J. Geophys. Res. 122, 1274–1296. https://doi.org/10.1002/2016JC012366
Lanckriet, T.M., Puleo, J.A., Masselink, G., Turner, I.L., Conley, D.C., Blenkinsopp, C., Russell, P., 2014. A comprehensive field study of swash-zone processes, Part 2: Sheet flow sediment concentrations during quasi-steady backwash. J. Waterw. Port Coast. Ocean Eng. 140, 29–42.
Masselink, G., Evans, D., Hughes, M.G., Russell, P., 2005. Suspended sediment transport in the swash zone of a dissipative beach. Mar. Geol. 216, 169–189.
Masselink, G., Pattiaratchi, C.B., 1998. The effect of sea breeze on beach morphology, surf zone hydrodynamics and sediment resuspension. Mar. Geol. 146, 115–135.
Masselink, G., Puleo, J.A., 2006. Swash-zone morphodynamics. Cont. Shelf Res. 26, 661–680.
Masselink, G., Russell, P., 2006. Flow velocities, sediment transport and morphological change in the swash zone of two contrasting beaches. Mar. Geol. 227, 227–240.
Masselink, G., Russell, P., Turner, I., Blenkinsopp, C., 2009. Net sediment transport and morphological change in the swash zone of a high-energy sandy beach from swash event to tidal cycle time scales. Mar. Geol. 267, 18–35.
Meyer-Peter, E., Muller, R., 1948. Formulas for bed-load transport. Presented at the Proceedings 3rd Meeting of the International Association for Hydraulic Research, pp. 39–64.
Miles, J., Butt, T., Russell, P., 2006. Swash zone sediment dynamics: A comparison of a dissipative and an intermediate beach. Mar. Geol. 231, 181–200.

Musumeci, R.E., Marletta, V., Sanchez-Arcilla, A., Foti, E., 2018. A ferrofluid-based sensor to measure bottom shear stresses under currents and waves. J. Hydraul. Res. 56, 630–647.
O'Donoghue, T., Kikkert, G.A., Pokrajac, D., Dodd, N., Briganti, R., 2016. Intra-swash hydrodynamics and sediment flux for dambreak swash on coarse-grained beaches. Coast. Eng. 112, 113–130.
O'Donoghue, T., Pokrajac, D., Hondebrink, L.J., 2010. Laboratory and numerical study of dambreak-generated swash on impermeable slopes. Coast. Eng. 57, 513–530.
Pintado-Patino, J.C., Torres-Freyermuth, A., Puleo, J.A., Pokrajac, D., 2015. On the role of infiltration and exfiltration in swash zone boundary layer dynamics in the swash zone. J. Geophys. Res. 120, 6329–6350. https://doi.org/10.1002/2015JC010806
Puleo, J.A., Beach, R.A., Holman, R.A., Allen, J.S., 2000. Swash zone sediment suspension and transport and the importance of bore-generated turbulence. J. Geophys. Res. 105, 17021–17044.
Puleo, J.A., Blenkinsopp, C., Conley, D.C., Masselink, G., Turner, I.L., Russell, P., Buscombe, D., Howe, D., Lanckriet, T.M., McCall, R.T., Poate, T., 2014a. A comprehensive field study of swash-zone processes, Part 1: Experimental design with examples of hydrodynamic and sediment transport measurements. J. Waterw. Port Coast. Ocean Eng. 140, 14–28.
Puleo, J.A., Holland, K.T., 2001. Estimating swash zone friction coefficients on a sandy beach. Coast. Eng. 43, 25–40.
Puleo, J.A., Lanckriet, T., Conley, D.C., Foster, D.L., 2015. Sediment transport partitioning in the swash zone of a large-scale laboratory beach. Coast. Eng. https://doi.org/doi:10.1016/j.coastaleng.2015.11.001
Puleo, J.A., Lanckriet, T.M., Blenkinsopp, C., 2014b. Bed level fluctuations in the inner surf and swash zone of a dissipative beach. Mar. Geol. 349, 99–112.
Puleo, J.A., Lanckriet, T.M., Wang, P., 2012. Nearbed cross-shore velocity profiles, bed shear stress and friction on the foreshore of a microtidal beach. Coast. Eng. 68, 6–16.
Puleo, J.A., Torres-Freyermuth, A., 2016. The second international workshop on swash-zone processes. Coast. Eng. 115, 1–7. https://doi.org/10.1016/j.coastaleng.2015.09.007
Raubenheimer, B., 2002. Observations and predictions of fluid velocities in the surf and swash zones. J. Geophys. Res. 107.
Raubenheimer, B., Elgar, S., Guza, R.T., 2004. Observations of swash zone velocities: A note on friction coefficients. J. Geophys. Res. 109, C01027, doi:10.1029/2003JC001877.
Raubenheimer, B., Guza, R.T., 1996. Observations and predictions of run-up. J. Geophys. Res. 101, 25575–25587.
Raubenheimer, B., Guza, R.T., Elgar, S., Kobayashi, N., 1995. Swash on a gently sloping beach. J. Geophys. Res. 100, 8751–8760.
Roelvink, J.A., McCall, R.T., Seyedabdolhossein, M., Nederhoff, K., Dastgheib, A., 2018. Improving predictions of swash dynamics in XBeach: The role of groupiness and incident-band runup. Coast. Eng. J. 134, 103–123.
Shen, M.C., Meyer, R.E., 1963. Climb of a bore on a beach: Part 3, run-up. J. Fluid Mech. 16, 113–125.
Shen, M. C., Meyer, R.E., 1963. Climb of a bore on a beach: Part 2, Non-uniform beach slope. J. Fluid Mech. 16, 108–112.
Smyth, C., Hay, A.E., 2003. Near-bed turbulence and bottom friction during SandyDuck97. J. Geophys. Res. 108, 3197. https://doi.org/doi:10.1029/2001JC000952

Swart, D.H., 1974. Offshore sediment transport and equilibrium beach profiles (No. Laboratory Publication No. 131). Delft Hydraulics.
Torres-Freyermuth, A., Puleo, J.A., DiCosmo, N., Allende-Arandia, M.E., Chardon-Maldonado, P., Lopez, J., Figueroa-Esponoza, B., Ruiz de Alegria Arzaburu, A., Figlus, J., Roberts, T.M., Candela, J., 2017. Nearshore circulation on a sea breeze dominated beach during intense wind events. Cont. Shelf Res. 151, 40–52. https://doi.org/10.1016/j.csr.2017.10.008
von Karman, T., 1931. Mechanical Similitude and Turbulence (Technical Memorandum No. NACA-TM, No .611). National Advisory Committee for Aeronautics, Washington, D.C.
Wang, P., Ebersole, B.A., Smith, E.R., 2002. Longshore sand transport - Initial results from large scale sediment transport facility (No. ERDC/CHL CHETN-II-46). USACE.
Wilson, K.C., 1989a. Friction of wave-induced sheet flow. Coast. Eng. 12, 371–379.
Wilson, K.C., 1989b. Mobile-bed friction at high shear stress. J. Hydraul. Eng. 115, 825–830.
Wright, L.D., Guza, R.T., Short, A.D., 1982. Dynamics of a high-energy dissipative surf zone. Mar. Geol. 45, 41–62.

766

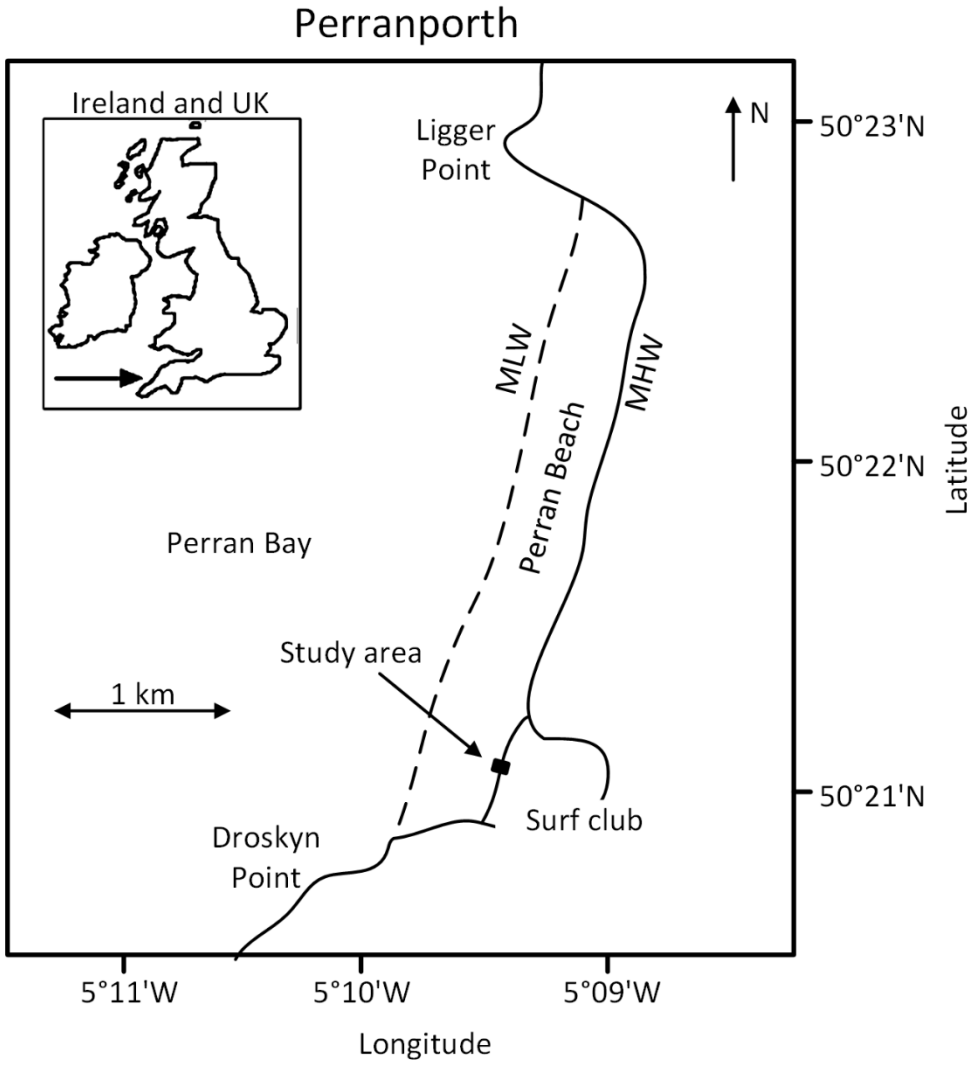

767

768 Figure 1. Map showing Perran Beach in Perranporth, Cornwall on the southwest coast of

769 England. The study area is defined by the small black box spanning the mean high water line.

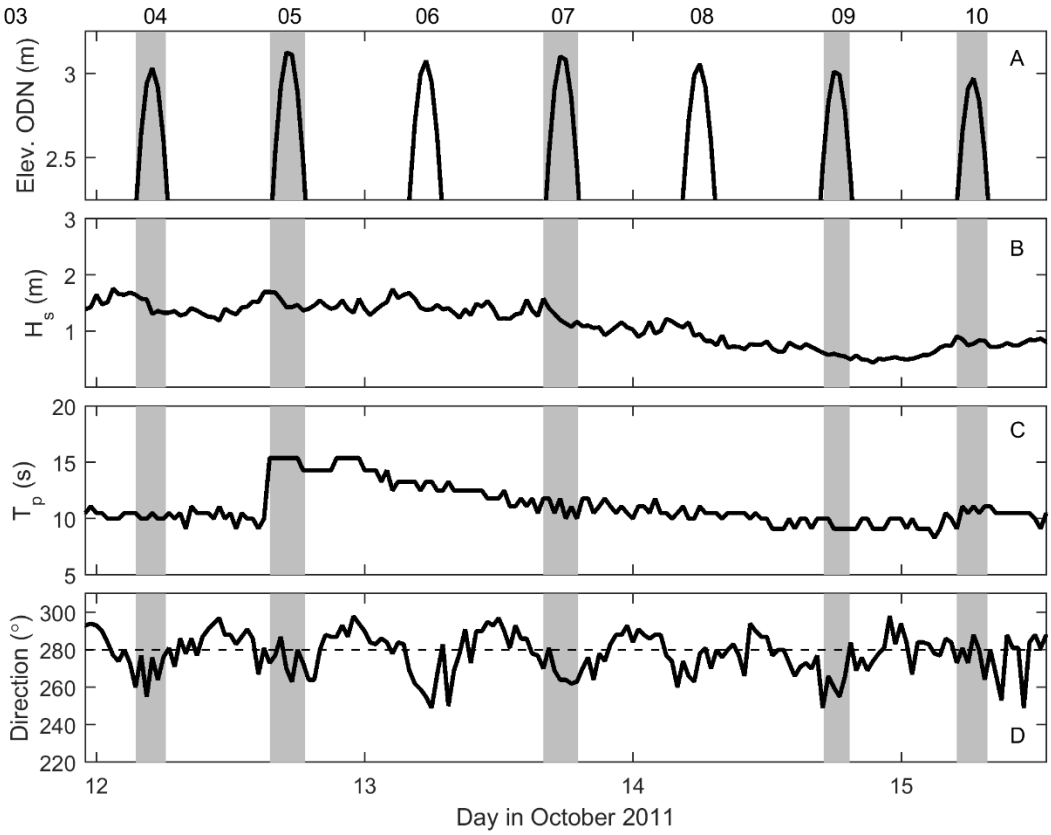

770

771 Figure 2. Conditions at Perran Beach during the study. A) Tide level, B) Significant wave height,
772 C) Spectral peak period, and D) Wave direction. The horizontal dashed line in (D) represents
773 shore normal wave angle of incidence. The gray shading identifies the sampling duration for
774 Tides 4, 5, 7,9, and, 10 where the tide number is shown on the upper axis of panel (A).

775

776 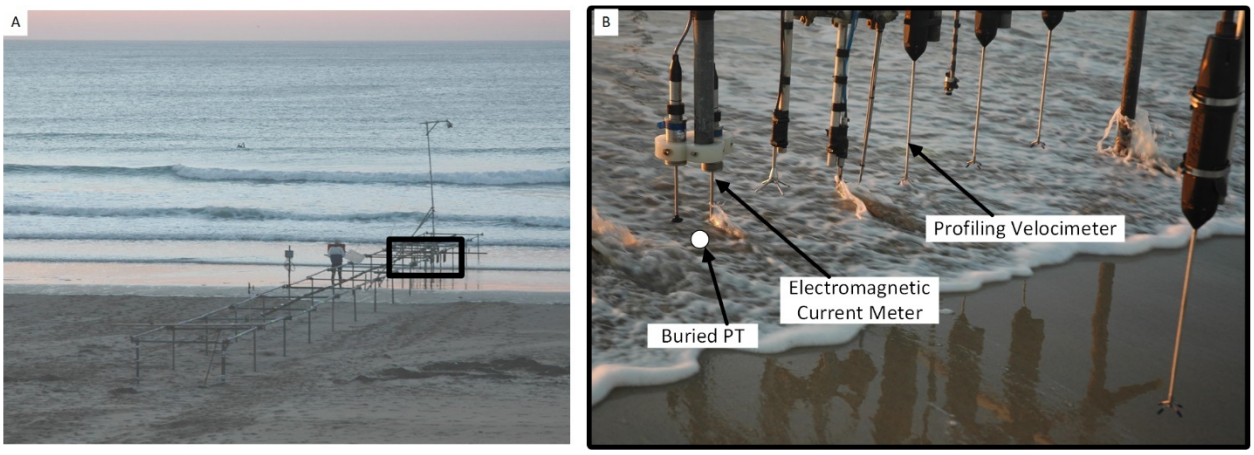

777 Figure 3. A) Image of the scaffold frame prior to high tide. The black box identifies the location
778 of the deployed sensors used in this paper. B) The sensors deployed during the BeST study. Only
779 the lower Electromagnetic current meter (EM) and lower Profiling Velocimeter were used in this
780 paper. Buried pressure transducers were located under the EM pair.

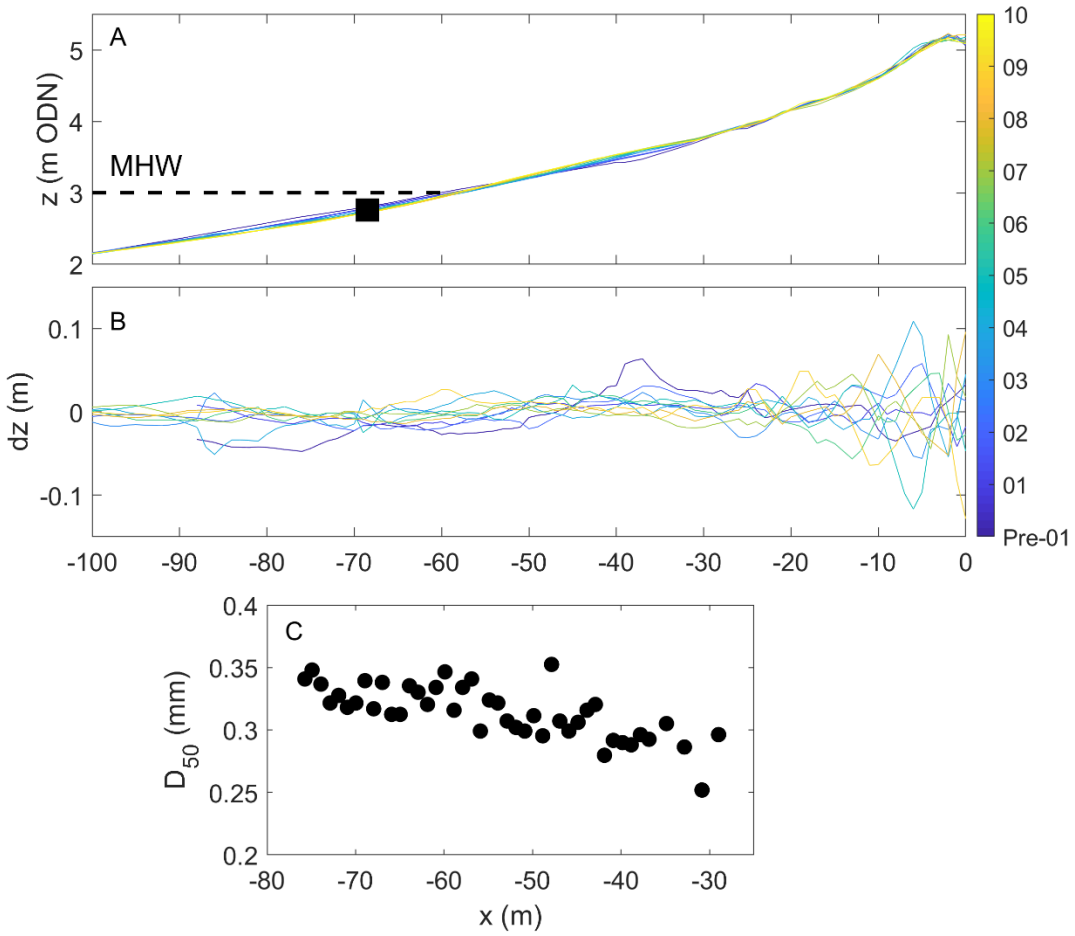

781

782 Figure 4. A) Beach profiles collected along the scaffold frame center line. The black symbol
783 indicates the locations of sensors and the color scale indicates the Tide number. B) Elevation
784 differences between adjacent profiles (e.g. Tide 2 – Tide 1). C) Median grain size within the
785 cross-shore expanse of the scaffold frame.

786

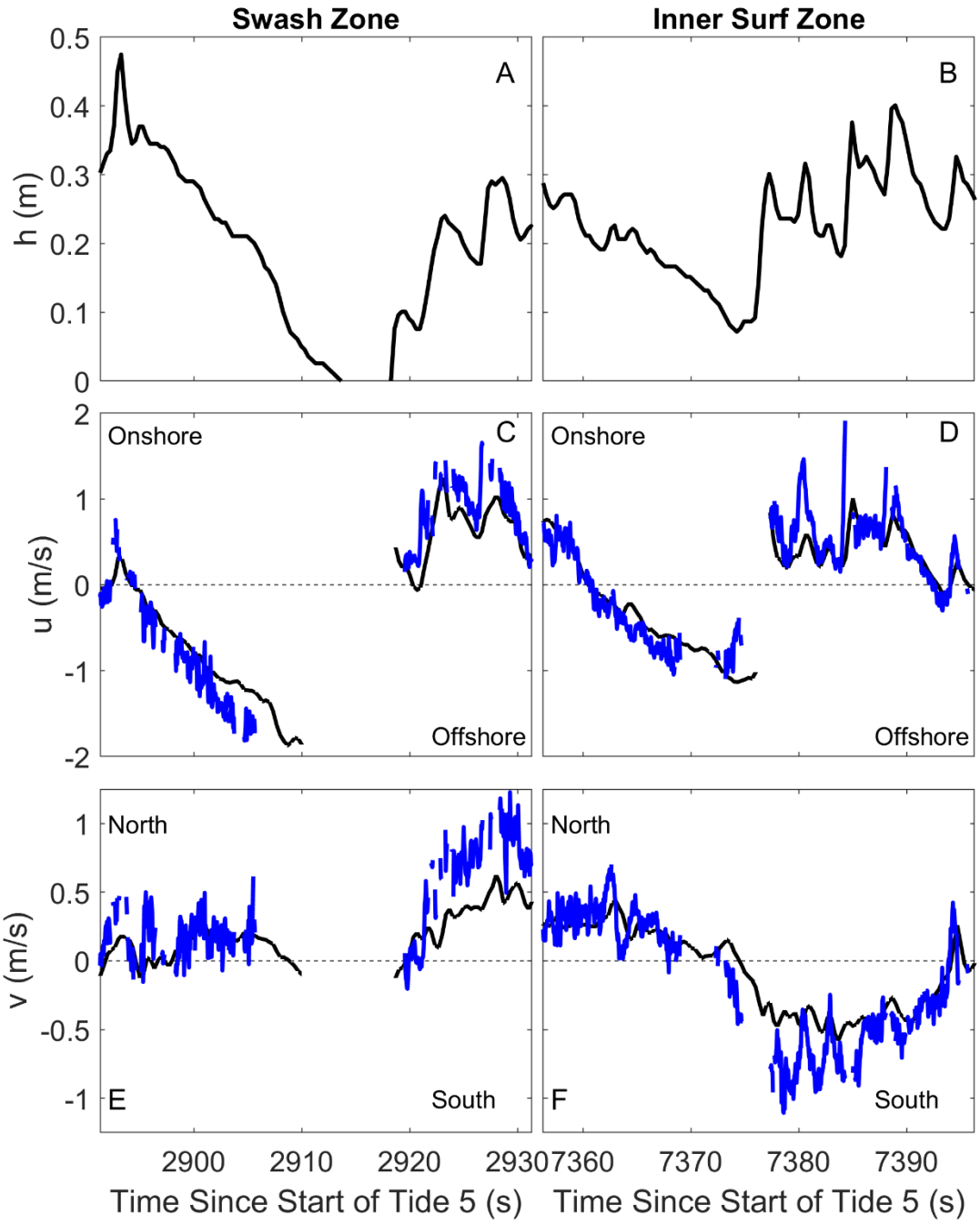

787

788 Figure 5. Example time series excerpt from Tide 5 showing data from the swash zone (left

789 column) and inner surf zone (right column). A,B) Water depth. C,D) Cross-shore velocity. E,F)

790 Alongshore velocity. EM data are shown in black and PV data in blue.

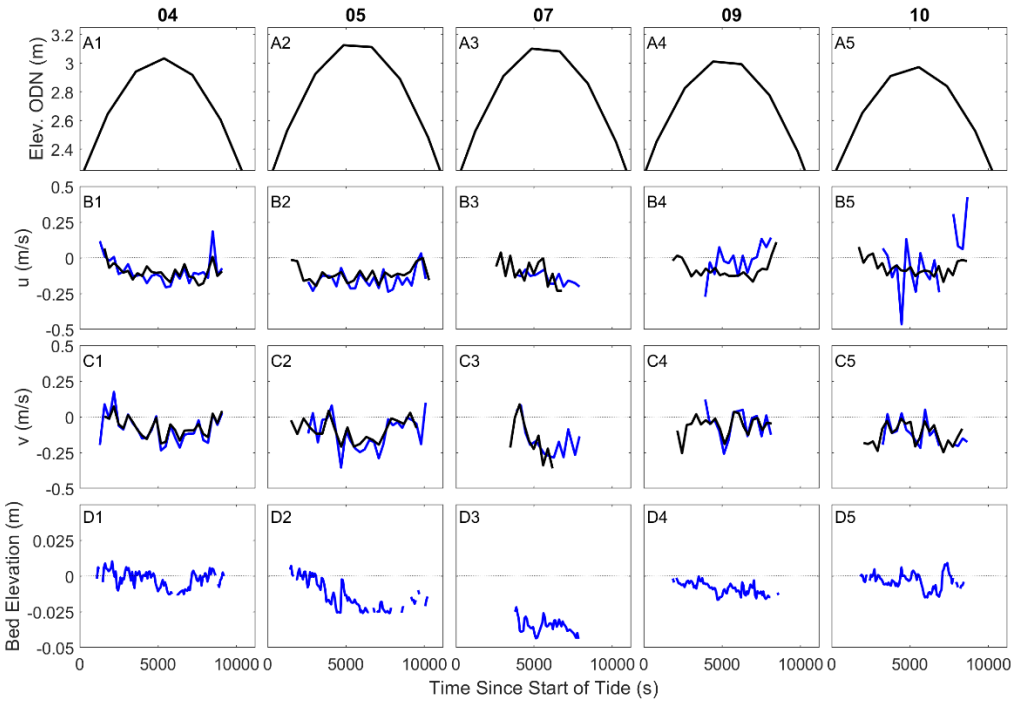

791

792 Figure 6. Tidal overview (5-minute average) of conditions during the study. A1-A5) Water level.

793 B1-B5) Cross-shore velocity. C1-C5) Alongshore velocity. D1-D5) Bed elevation. EM data are

794 shown in black and PV data in blue.

795

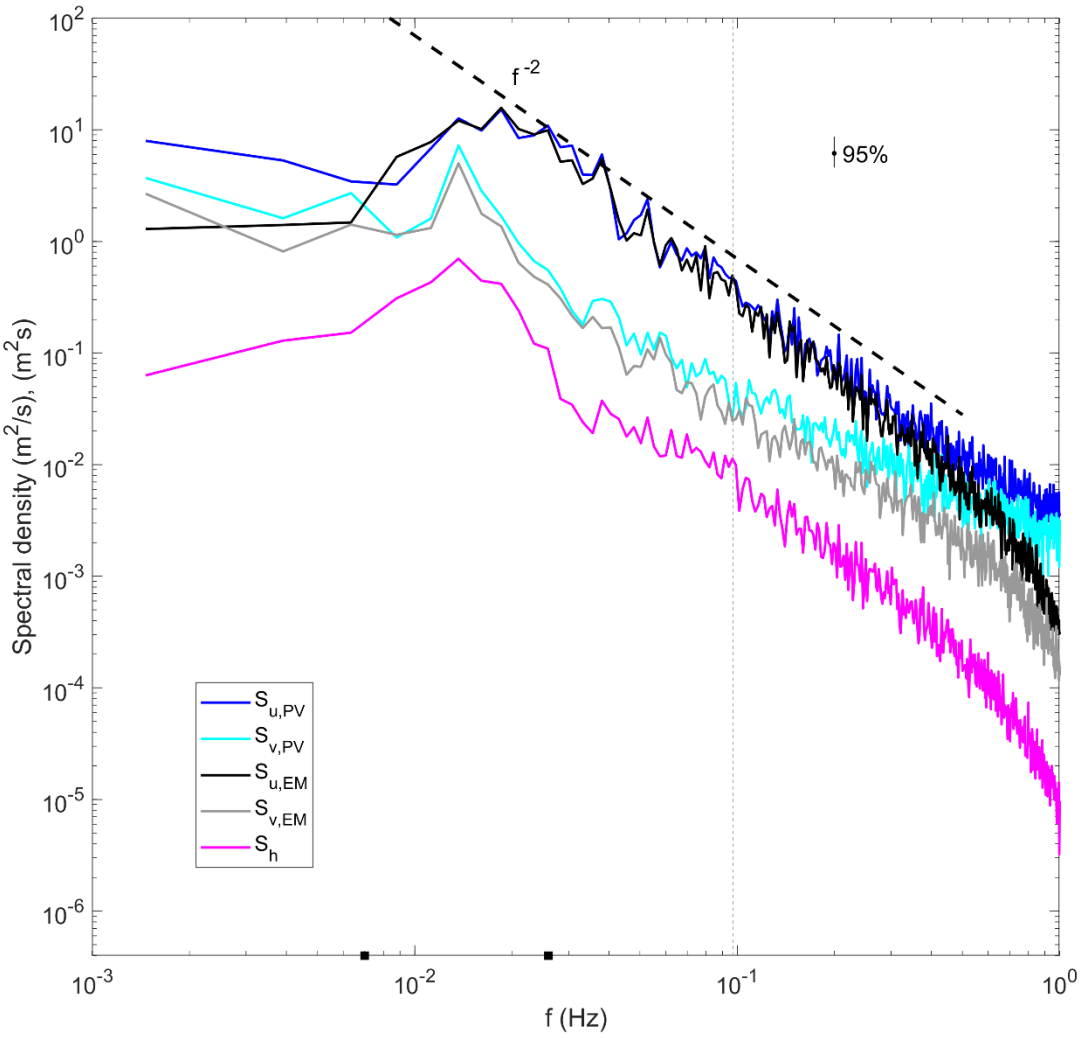

796

797 Figure 7. Example spectra from Tide 10. The vertical dotted line is the offshore spectral peak

798 wave frequency. The f^{-2} slope and 95% confidence interval are shown.

799

800

801

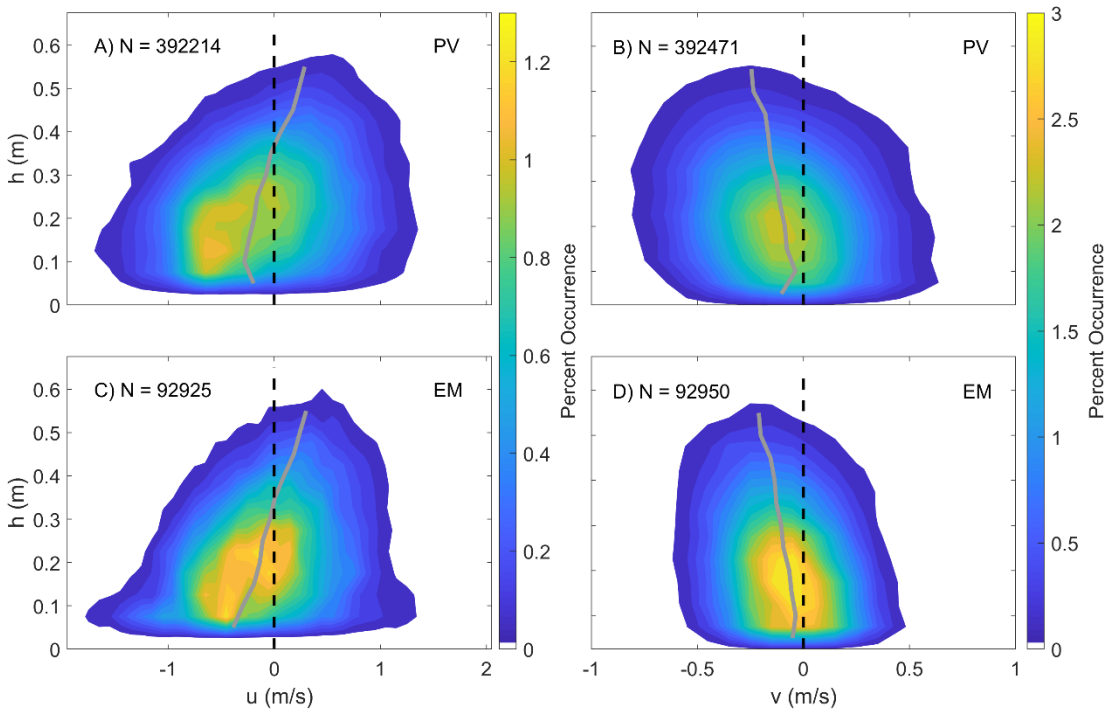

802

803 Figure 8. Two-dimensional histograms of water depth and velocity (cross-shore; left column,
804 alongshore; right column). A,B) Velocity from the PV. C,D) Velocity from the EM. The color
805 scale indicates the percent occurrence (occurrence < 0.1% forced to zero for visual clarity). The
806 gray line represents the mean velocity for each water depth bin and the dashed black line
807 identifies the change in flow direction. The number of data points (N) is included in each panel.

808

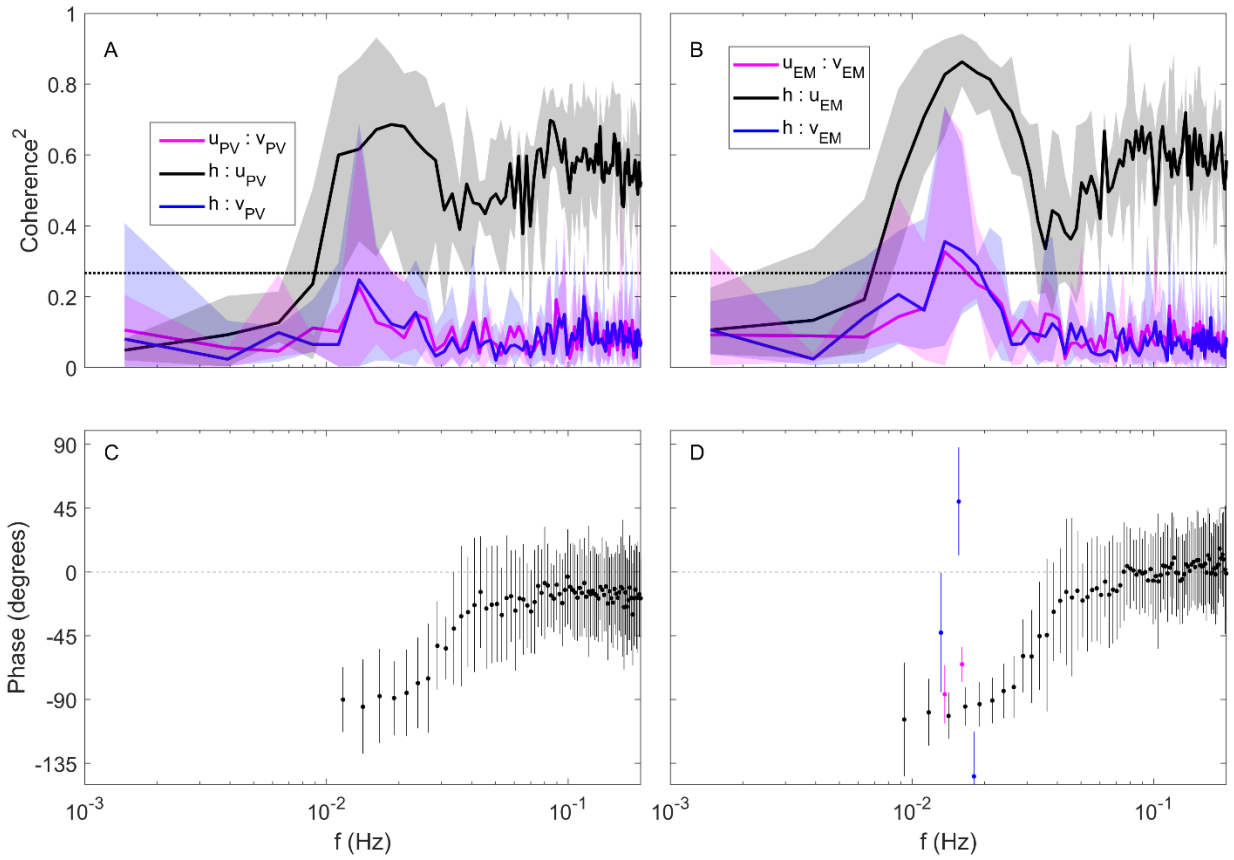

809

810

811 Figure 9. Averaged cross-spectra squared coherence for velocity and depth (A in relation to PV;
812 B in relation to EM). Shading indicates minimum and maximum values for the five tides. The
813 horizontal dotted line denotes the 95% confidence level. C,D) Phase with 95% confidence limits.
814 Phase is shown when squared coherence is significant.

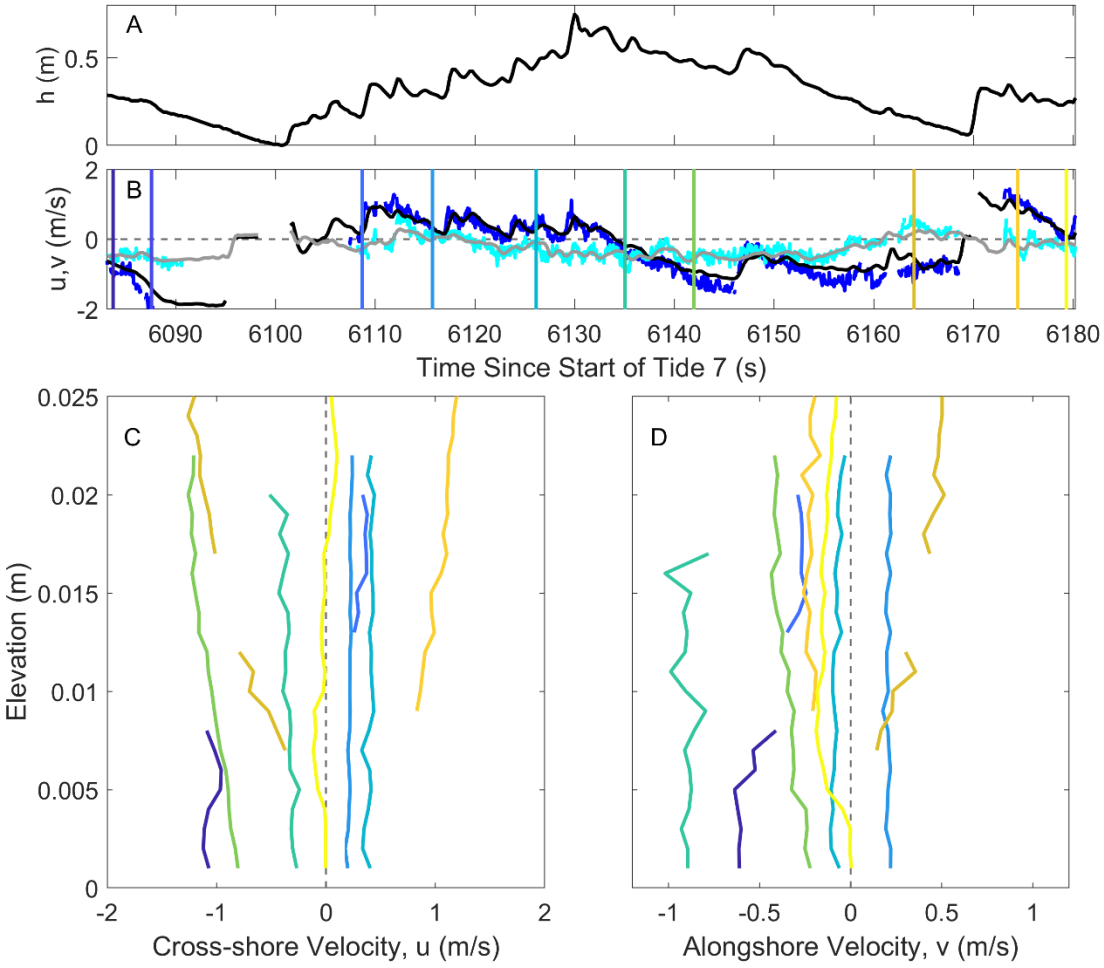

Figure 10. Example time series excerpt of a swash zone infragravity event from Tide 7. A) Water depth. B) Cross-shore (black: EM; blue: PV) and alongshore (grey: EM; cyan: PV) velocity. C,D) Vertical profiles of cross-shore (C) and alongshore (D) velocities at different portions of the excerpt as identified by the color shading in (B).

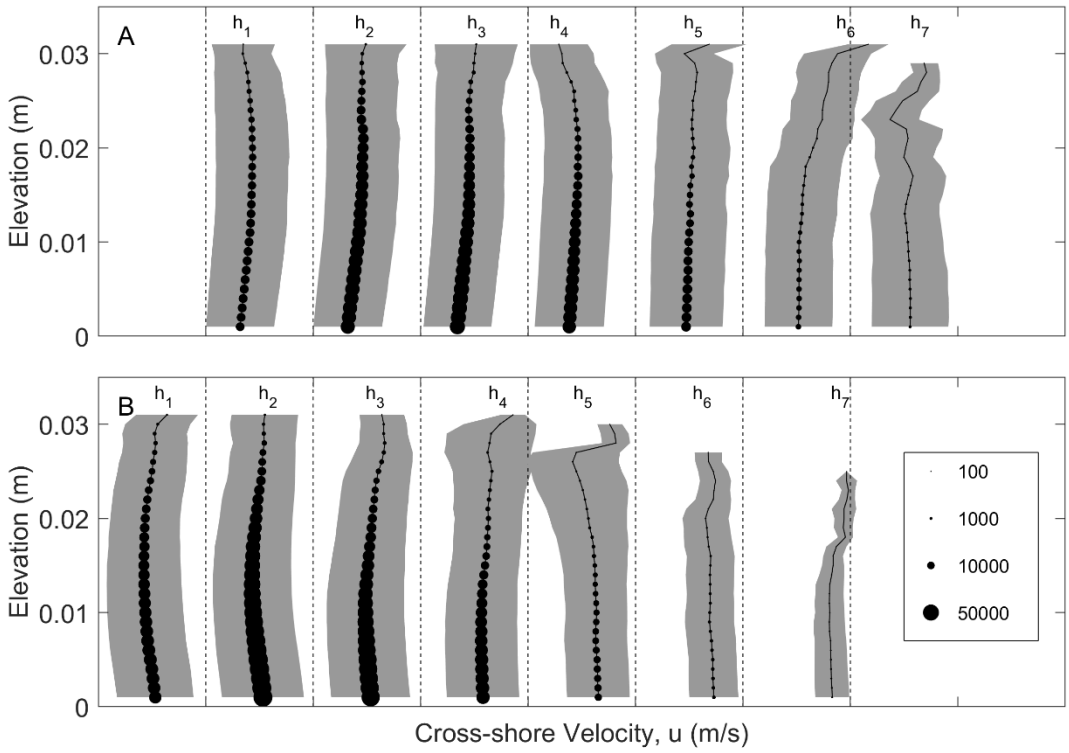

Figure 11. Time-averaged cross-shore velocity profiles as a function of depth bin (Table 3; h_1: 0 – 0.1 m; h_2: 0.1 – 0.2 m; h_3: 0.2 – 0.3 m; h_4: 0.3 – 0.4 m; h_5: 0.4 – 0.5 m; h_6: 0.5 – 0.6 m; h_7: 0.6 – 0.7 m). A) Onshore-directed flow. B) Offshore-directed flow. Profiles are offset for visual clarity by 1 m/s in the horizontal as denoted by the vertical dashed lines. Onshore-directed flows are to the right of the dashed lines and offshore-directed flows are to the left. The color shading represents one standard deviation either side of the mean. The symbol size in the legend signifies the number of data points used in the averaging procedure.

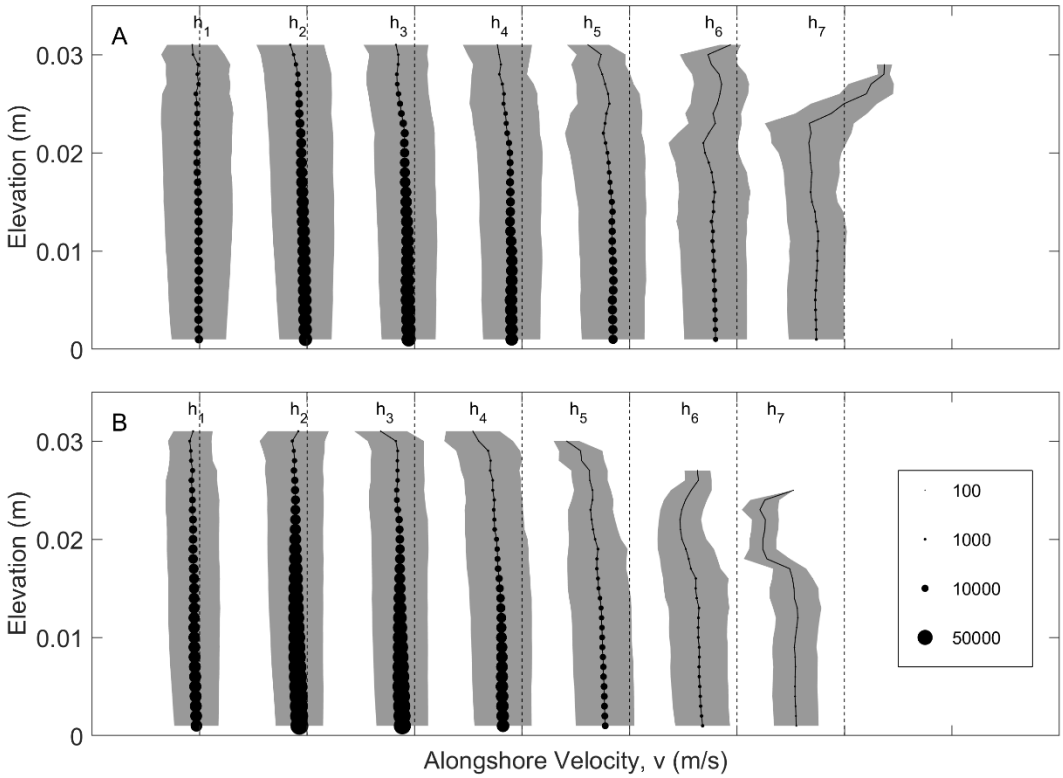

832

833 Figure 12. Time-averaged alongshore velocity profiles as a function of depth bin (Table 3; h_1: 0
834 – 0.1 m; h_2: 0.1 – 0.2 m; h_3: 0.2 – 0.3 m; h_4: 0.3 – 0.4 m; h_5: 0.4 – 0.5 m; h_6: 0.5 – 0.6 m; h_7: 0.6
835 – 0.7 m). A) Alongshore flows during onshore-directed motion. B) Alongshore flows during
836 offshore-directed motion. Profiles are offset for visual clarity by 1 m/s in the horizontal as
837 denoted by the vertical dashed lines. Northerly-directed flows are to the right of the dashed lines
838 and southerly-directed flows are to the left. The color shading represents one standard deviation
839 either side of the mean. The symbol size in the legend signifies the number of data points used in
840 the averaging procedure.

841

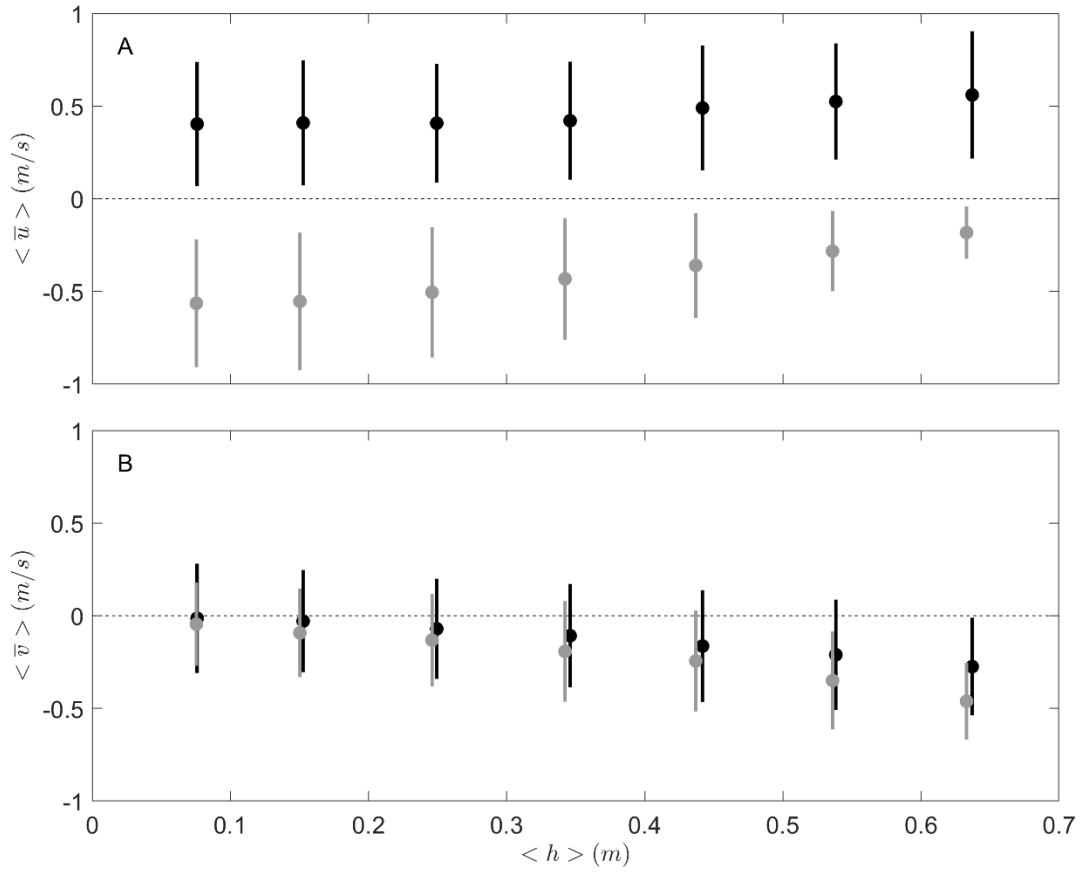

Figure 13. Temporal mean of the depth-averaged velocities as a function of mean water depth (depth bin) (Table 3). A) Cross-shore velocity. B) Alongshore velocity. Black (grey) symbols are onshore-directed (offshore-directed) velocity or alongshore velocities during onshore-directed (offshore-directed) motion. Vertical bars represent one standard deviation either side of the mean.

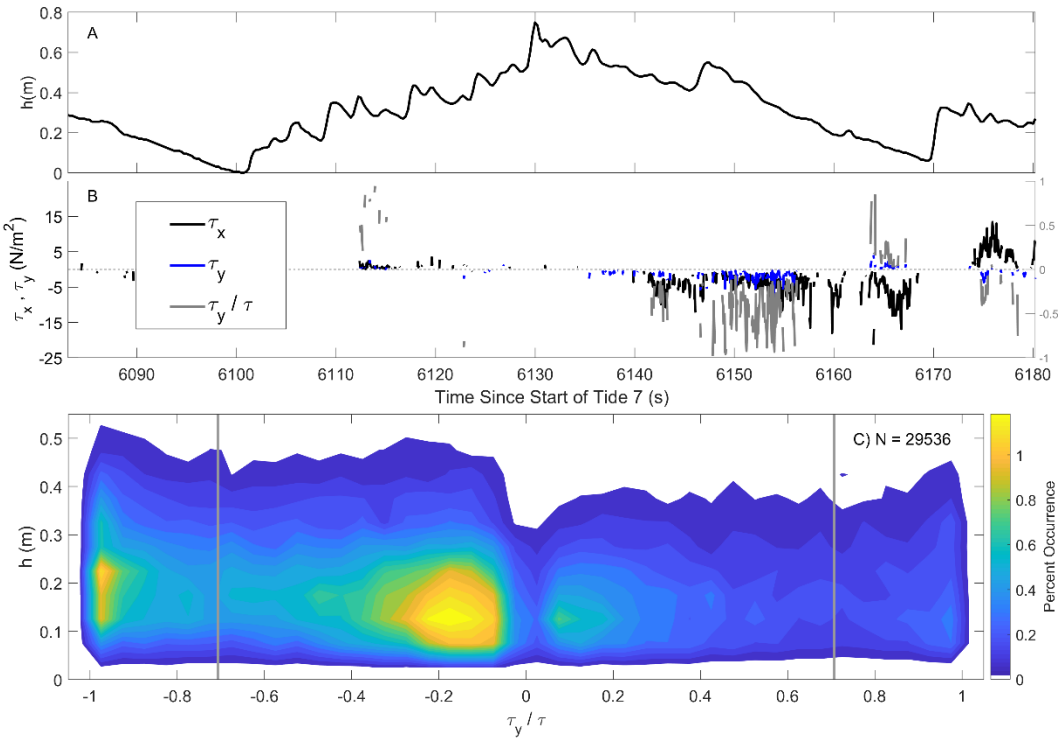

848

849 Figure 14. A) Example time series excerpt for water depth from an infragravity event from Tide
850 7. B) Corresponding bed shear stress for cross-shore (black) and alongshore (blue) motion. The
851 ratio of alongshore bed shear stress to total bed shear stress is shown in grey and uses the right
852 vertical axis. C) Two-dimensional histogram of the water depth and ratio of alongshore bed shear
853 stress to total bed shear stress. The color scale indicates the percent occurrence and the grey
854 vertical lines demarcate when the alongshore bed shear stress component dominates.

855

856

857

858

859

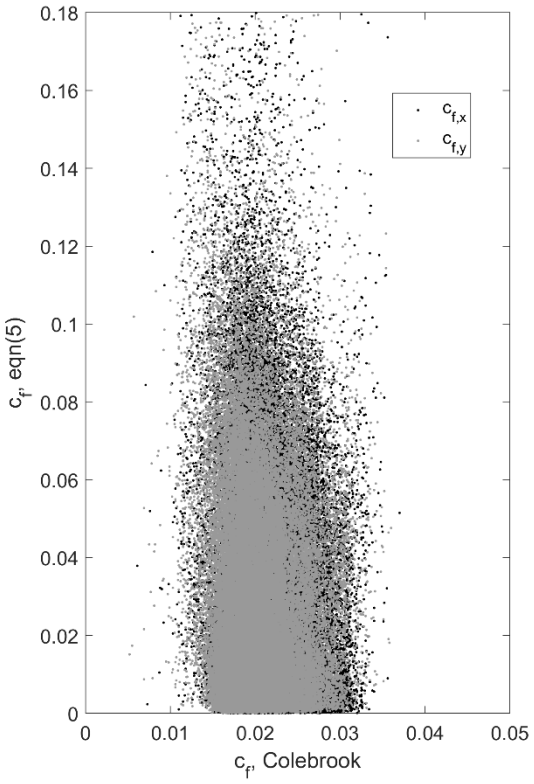

Figure 15. Comparison of the friction coefficient estimated from the Colebrook formulation and that estimated from the Law of the Wall (equation 5).

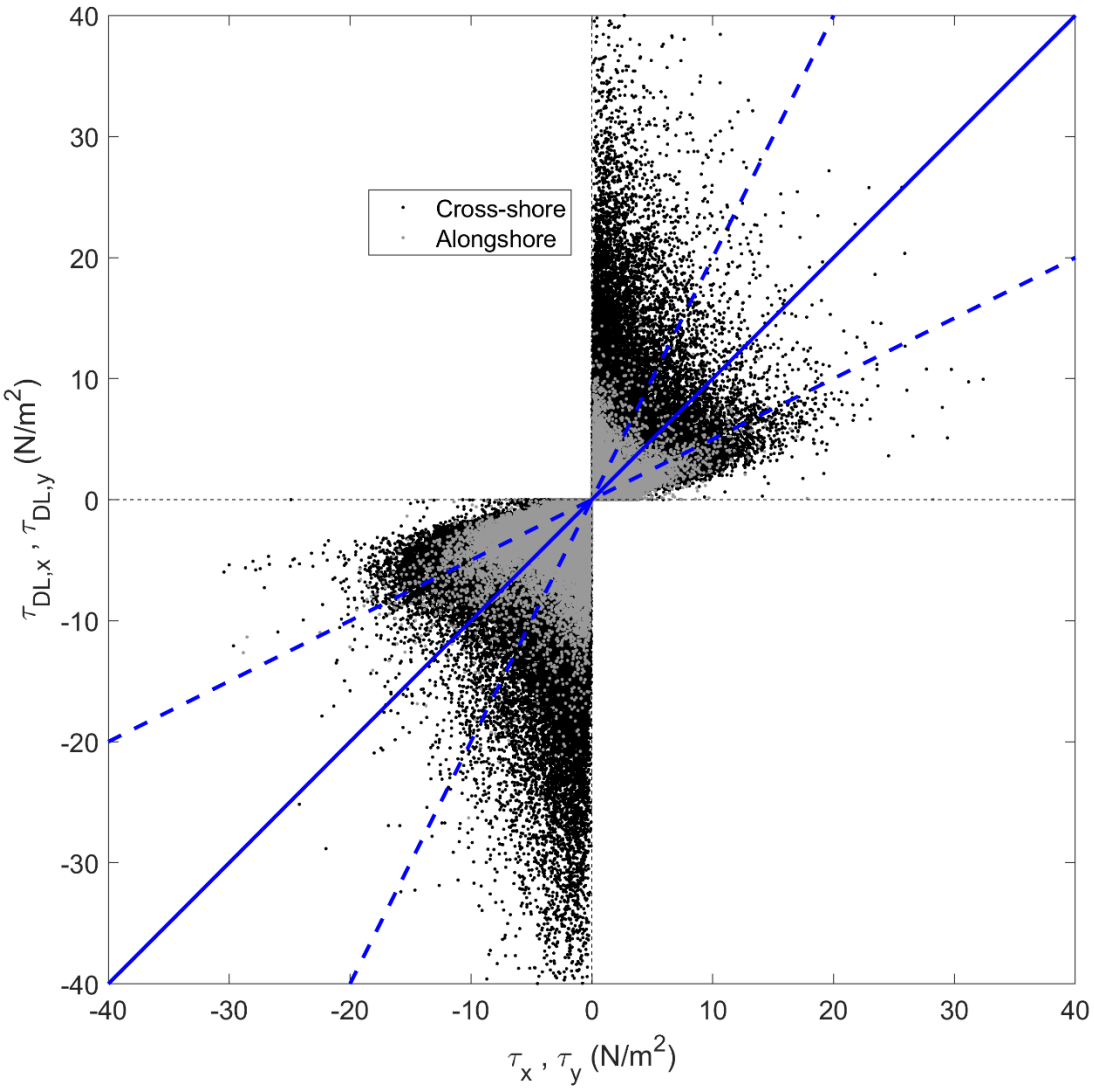

867

868 Figure 16. Comparison of the shear stress from the Law of the Wall to that estimated from the
869 quadratic drag law, (τ_{DL}). The solid blue line is the line of perfect agreement (1 – 1). The dashed
870 blue lines are a factor of 2 difference. Black symbols are for cross-shore-directed flows. Grey
871 symbols are for alongshore-directed flows.

872

873

874

875

876 Table 1. Spectral peak frequency and period for velocity and depth for each tide.

	TIDE4	TIDE5	TIDE7	TIDE9	TIDE10
$P_{u,PV}$ (s^{-1}, [s])	0.023	0.033	0.028	0.019	0.019
	[43.5]	[30.3]	[35.7]	[52.6]	[52.6]
$P_{v,PV}$ (s^{-1} [s])	0.014	0.033	0.026	0.019	0.019
	[71.4]	[30.3]	[38.5]	[52.6]	[52.6]
$P_{u,EM}$ (s^{-1}, [s])	0.023	0.019	0.019	0.016	0.014
	[43.5]	[52.6]	[52.6]	[62.5]	[71.4]
$P_{v,EM}$ (s^{-1}, [s])	0.014	0.019	0.014	0.016	0.014
	[71.4]	[52.6]	[71.4]	[62.5]	[71.4]
P_h (s^{-1}, [s])	0.014	0.019	0.014	0.016	0.014
	[71.4]	[52.6]	[71.4]	[62.5]	[71.4]

877

878

879

880 Table 2. Percent of spectral energy density contained in the infragravity band.

	TIDE4	TIDE5	TIDE7	TIDE9	TIDE10
$\%IG_{u,PV}$	76	71	73	71	81
$\%IG_{v,PV}$	74	72	72	74	83
$\%IG_{u,EM}$	77	71	93	73	83
$\%IG_{v,EM}$	77	72	92	83	88
$\%IG_{h}$	78	62	80	72	87

881

882

883

884

885 Table 3. Mean depth, mean of depth-averaged velocities and the degree of uniformity of velocity
886 profiles for different depth bins.

	h_1	h_2	h_3	h_4	h_5	h_6	h_7
Bin range (m)	(0 - 0.1]	(0.1 - 0.2]	(0.2 - 0.3]	(0.3 - 0.4]	(0.4 - 0.5]	(0.5 - 0.6]	(0.6 - 0.7]
$<h>$ for u_{on} , v_{on}	0.076	0.152	0.25	0.35	0.44	0.54	0.64
$<h>$ for u_{off}, v_{off}	0.075	0.15	0.25	0.34	0.44	0.54	0.63
$\overline{< u_{on} >}$	0.40	0.41	0.41	0.42	0.49	0.52	0.56
$\overline{< u_{off} >}$	-0.56	-0.55	-0.50	-0.43	-0.36	-0.28	-0.18
$\overline{< v_{on} >}$	-0.01	-0.03	-0.07	-0.11	-0.16	-0.21	-0.27
$\overline{< v_{off} >}$	-0.05	-0.09	-0.13	-0.19	-0.24	-0.35	-0.46
$B_{u,on}$	0.05	0.06	0.06	0.06	0.06	0.23	0.08
$B_{u,off}$	0.08	0.07	0.10	0.10	0.12	0.03	0.09
$B_{v,on}$	0.02	0.05	0.05	0.06	0.07	0.06	0.27
$B_{v,off}$	0.02	0.02	0.05	0.10	0.13	0.09	0.17

887

888

889

890

891

892